EARTH SURFACE PROCESSES AND LANDFORMS
Earth Surf. Process. Landforms **45**, 978–998 (2020)

Published online 7 January 2020 in Wiley Online Library
(wileyonlinelibrary.com) DOI: 10.1002/esp.4791

Modelling scour and deposition in harbours due to complex tsunami-induced currents

Sangyoung Son,[1]* Patrick Lynett[2] and Aykut Ayca[2]
[1] School of Civil, Environmental and Architectural Engineering, Korea University, Seoul 02841, Republic of Korea
[2] Sonny Astani Department of Civil and Environmental Engineering, University of Southern California, Los Angeles, CA 90089, USA

Received 2 April 2019; Revised 3 December 2019; Accepted 4 December 2019

*Correspondence to: Sangyoung Son, School of Civil, Environmental and Architectural Engineering, Korea University, Seoul 02841, Republic of Korea.
E-mail: sson@korea.ac.kr

ESPL
Earth Surface Processes and Landforms

ABSTRACT: In this paper, a set of models responsible for hydrodynamics, sediment transport, and morphological evolution are introduced with their theoretical backgrounds, and it is explained how they are fully connected through a two-way coupling to yield an integrated sediment transport model applicable to tsunami cases. In particular, a fully nonlinear Boussinesq model with bottom shear-induced rotational terms is chosen for the hydrodynamic model in order to provide a better physical approximation of tsunami-related, near-bed hydrodynamics in the nearshore. A finite-volume scheme, stable and suitable for phase-resolving model runs longer than 10 simulated hours, is adopted in the numerical discretization. The accuracy and applicability of the developed model are investigated through numerical tests on various sediment problems in the shallow region. Calculated results agree well with existing experimental records. Finally, an ocean-wide, field-scale simulation of the 2011 Tohoku-oki tsunami is attempted, with a focus on the localized effects of tsunami-induced morphological changes at Crescent City Harbor and Santa Cruz Harbor (USA). Consistent with the reported observations, strong and vortical velocity fields are generated through the model and result in significant changes in morphological configurations. Depth variations and areas of scouring and deposition are compared between modelled and observed records, and the results are discussed. © 2019 John Wiley & Sons, Ltd.

KEYWORDS: tsunami-induced current; scouring; deposition; sediment transport; finite-volume method; Boussinesq model

Introduction

Tsunamis have had enormous impacts on both near-field and far-field coastal areas and the relevant issues focus mainly on the hazards due to their hydraulics, for example, strong currents and inundation. However, another imprint that tsunamis leave behind on the coast is geomorphological change (Nishimura and Miyaji, 1995; Dawson and Shi, 2000; Scheffers and Kelletat, 2003; Moore *et al.*, 2006; Paris *et al.*, 2009; Wilson *et al.*, 2012; Engel *et al.*, 2016). Accordingly, attention is drawn to the tsunami-induced sediment transport, and this forms another focus of tsunami research (Apotsos *et al.*, 2011; Goto *et al.*, 2011; Sugawara *et al.*, 2014; Yamashita *et al.*, 2016; Yoshii *et al.*, 2017).

Sediment transport processes caused either by tsunami waves or by wind waves are often complex and multi-scale, requiring interpretation from a variety of disciplines (Horikawa, 1981; Sugawara *et al.*, 2014), including hydrodynamics, morphodynamics, meteorology, geology, and ecology. Tsunami-induced nearshore hydrodynamics tend to be especially chaotic and unpredictable due to the existence of various types of diffusive sources [e.g. bottom boundary shear in Lynett *et al.* (2012), wave breaking in Yoon and Cox (2010), active sedimentation in Cheng and Weiss (2013)], and significant uncertainty remains about sediment processes (Elfrink and Baldock, 2002; Jaffe *et al.*, 2016). Shoreline evolution induced by tsunami waves can have a negative impact on both human structures and marine ecosystems; scouring near coastal structures (Tomita *et al.*, 2006), sediment deposits in harbour basins and navigation channels, beach loss, and loss of habitat for marine species. The impact becomes much greater when it occurs in a heavily populated coastal region (e.g. Saengsupavanich *et al.*, 2009; Wilson *et al.*, 2012).

The nearshore hydrodynamics modelling with high accuracy, especially for long tsunami waves, is essential to predicting sediment transport in coastal regions; modelling techniques at present are based on various theoretical and numerical backgrounds. Admitting that tsunami deposits mutually affect tsunami hydrodynamics and inundation extent, the use of hydrodynamic models with higher level of accuracy seems to be natural (e.g. Cheng and Weiss, 2013). Papanicolaou *et al.* (2008) provided a thorough overview of existing morphodynamic models, their applicability, and limitations. Sugawara *et al.* (2014) reviewed the attempts in tsunami sediment transport modelling. Elfrink and Baldock (2002) covered the general fundamentals of sediment processes in the swash zone. Generally, the sediment problem is numerically approached by constructing an integrated model composed of three sub-models: nearshore hydrodynamics, morphodynamics, and sediment transport (Rakha *et al.*, 1997; Karambas and Koutitas, 2002; Cao *et al.*, 2004; Karambas, 2006; Castro Díaz *et al.*, 2008; Wu and Wang, 2008; Kim

and Lee, 2012; Li *et al.*, 2012; Sugawara *et al.*, 2014). Representing the surrounding physics and coupled within an integrated model, each sub-model is capable of simulating sediment processes in dynamic environments where a shallow flow field interacts with the sediment boundary, resulting in sea floor changes.

The majority of sediment models used in coastal regions are assumed to be governed by flows in the shallow water regime, which eliminates the depth dependency of the flow and increases computational efficiency. Generally, sediments start to move by fluid motion at about 150–200 m water depth (Horikawa, 1981), and the employment of a shallow water equation on sediment modelling is valid (e.g. Alsina *et al.*, 2009; Li *et al.*, 2012; Postacchini *et al.*, 2012). However, a more complicated flow regime is expected in the surf and swash zones because of the complex hydraulic situations that will sometimes be encountered, including: wave breaking; wave runup/rundown; undular bores; turbulent interactions between wave-current, wave-bottom, and wave-structure; freshwater/seawater mixing, and so on. Thus, shallow water models cannot guarantee the accuracy of predictions in nearshore areas (Raubenheimer, 2002; Bakhtyar *et al.*, 2009).

The attempt to overcome these limitations has resulted in another branch of nearshore hydrodynamic modelling: Boussinesq-type equations. This type of modelling is an expanded mathematical formulation of shallow water equations intended to address nearshore, higher-order effects from frequency dispersion and fluid rotationality as weak components (refer to Wei *et al.*, 1995; Kennedy *et al.*, 2000; Kim *et al.*, 2009; Son and Lynett, 2014). Here, 'high-order' terms indicate corrections to the nonlinear shallow water wave equations. The Boussinesq model is used to more precisely identify nearshore hydrodynamics by considering higher-order impacts to the flow field, which are increasingly important as waves approach the shoreline (Raubenheimer, 2002). Recent advances in the use of Boussinesq-type equations in tsunami modelling, with a focus on nearshore hydrodynamics, are shown in works by Grilli *et al.* (2007), Fuhrman and Madsen (2009), Son *et al.* (2011), Lynett *et al.* (2012), Borrero *et al.* (2015), and Kalligeris *et al.* (2016). Thus, coastal sediment modelling based on Boussinesq-type equations has resulted in more detailed descriptions of flow structure, making these equations more suitable for sediment transport calculations than those of other methods (e.g. Rakha *et al.*, 1997; Lawrence *et al.*, 2000; Karambas and Koutitas, 2002; Karambas, 2006; Shimozono *et al.*, 2007; Kim, 2015).

The purpose of this paper is to present an integrated numerical model developed to predict morphologic evolution caused by tsunami-induced currents in a nearshore area. Since the highly accurate prediction of nearshore currents is a key component in sediment modelling, and the dynamic environments are required to be accounted for, fully nonlinear Boussinesq equations equipped with various closure terms will be employed in the hydrodynamic calculation, while the empirically derived formulas for erosion and accretion will be incorporated in sediment transport equations. A finite-volume scheme, which enhances numerical stability in runs over 10 simulation hours, will be adopted for numerical discretizations of both Boussinesq and sediment transport equations.

This paper is organized as follows. First, theoretical details of Boussinesq equations, sediment transport equations, and morphologic evolution equations are presented with the closure models. Then, we introduce the numerical method for discretization of theoretical models. Numerical tests to examine the accuracy and applicability of the developed model are included. The model is applied to the 2011 Tohoku-oki tsunami, with a focus on the effects on sedimentation in Crescent City Harbor and Santa Cruz Harbor (USA). More general and detailed discussions on sedimentation caused by tsunami waves are made, with final conclusions summarized.

Theoretical Models

In the present study, separate sub-models are combined to create a complete system for modelling sediment processes in coastal areas. This integrated model is composed of three main parts: nearshore hydrodynamics, sediment transport, and morphologic evolution. Individual sub-models are outlined below, along with complete expressions for turbulent and sediment closures. The calculation procedure of the integrated model is also briefly discussed.

Nearshore hydrodynamic model: Boussinesq model

Accurate modelling of sediment transport is directly linked to the precise description of the flow field, and vice versa as explained in the Introduction. As tsunamis tend to induce complex hydrodynamics in the nearshore (Lynett *et al.*, 2012; Borrero *et al.*, 2015; Kalligeris *et al.*, 2016) and those are not well captured by typical shallow water models, the Boussinesq model is adopted as the hydrodynamic model component. Boussinesq equations are depth-integrated, phase-resolving equations (i.e. resolving the instantaneous wave orbital motions) for mass and momentum conservation in the shallow water regime and are widely used for nearshore hydrodynamic modelling. Recent developments include an expansion of the traditional fully nonlinear, weakly dispersive Boussinesq model based on potential theory (e.g. Wei *et al.*, 1995) to rotational flow (Kim *et al.*, 2009; Zhang *et al.*, 2013). Kim *et al.* (2009) have modified conventional equations for rotational fluid flows through the inclusion of bottom-induced turbulence effects as higher-order terms, which are balanced with dispersive effects. By means of various types of demonstrations, it is shown that the model can be used for more accurate predictions of nearshore modelling, which inherently involves complex surf and swash hydrodynamics [e.g. wave breaking, undular bores, runup/rundown in Kennedy *et al.* (2000), Bjørkavåg and Kalisch (2011)]. In terms of sediment modelling, the inclusion of bottom-induced rotationality into the model allows for a more reliable reconstruction of the velocity field by which sediment movements are initiated and controlled. Making use of rotational Boussinesq equations, an improved estimation of bed shear stress required for sediment transport calculations is achieved during the tsunami event.

Depth-integrated momentum and mass equations used in this study are as follows:

$$\frac{\partial H\widehat{u}_i}{\partial t}+\frac{\partial H\widehat{u}_i\widehat{u}_j}{\partial x_j}+gH\frac{\partial \zeta}{\partial x_i}+H\left(\mathscr{D}_i+\xi_i+\mathscr{D}_i^v+\xi_i^v\right)+\widehat{u}_i(\mathscr{M}+\mathscr{M}^v)-H\frac{\partial}{\partial x_j}\left(\nu_t^h\frac{\partial \widehat{u}_i}{\partial x_j}\right)+H\frac{\partial}{\partial x_i}\left(\nu_t^v\frac{\partial \widehat{u}_j}{\partial x_j}\right)+\frac{\tau_i^b}{\rho}-HF_i-HR_i=-\frac{(e-d)\widehat{u}_i}{1-p} \tag{1}$$

$$\frac{\partial H}{\partial t}+\frac{\partial H\widehat{u}_i}{\partial x_i}+(\mathscr{M}+\mathscr{M}^v)=\frac{e-d}{1-p} \tag{2}$$

where $i,j=(1,2)$, $H=\zeta+h$ is total water depth, ζ is surface elevation, h is water depth, and $\widehat{u}_i(=(\widehat{u},\widehat{v}))$ is velocity at depth

$\hat{z}(=-0.531h)$, e and d are sediment erosion and deposition fluxes, respectively, and p is bed porosity. $\mathscr{M}$ and $\mathscr{M}^v$ represent second-order correction terms due to frequency dispersion and bottom-induced turbulence effects, respectively, in the mass continuity. Similarly, $\mathscr{D}_i$ and $\mathscr{D}_i^v$ denote frequency dispersion and bottom-induced turbulence terms, respectively, in the momentum equation. Turbulent eddy viscosity is also included as ν_t^h and ν_t^v, which denote decomposed horizontal and vertical components, respectively, and τ_i^b is the shear stress on the bed. F_i is added to consider stochastic backscattering of energy from smaller to larger coherent structures. This enables the two-dimensional (2D) model to account for three-dimensional (3D) near-bed turbulence (Hinterberger *et al.*, 2007). The final term on the left side of the momentum equation, R_i, accounts for the effect of turbulent mixing and dissipation related to wave breaking (Chen *et al.*, 1999; Kennedy *et al.*, 2000).

In the above set of equations, the higher-order terms corresponding to ith-order perturbation terms with order $i>1$ represent the physical effects of scaling parameters as weakened with increasing order i. Accordingly, they distinguish rotational Boussinesq equations from potential-type equations and thus typical Boussinesq equations for potential theory are recovered through elimination of terms, $\mathscr{M}^v, \mathscr{D}_i^v, \xi_i^v$. Full descriptions for higher-order terms can be found in the online Supporting Information, while the other open expressions will be 'closed' by models given later in this paper (e.g. Kim, 2015).

It should be noted that some source terms (i.e. e and d) are added to the 'fixed-bed' Boussinesq model on the right side of Equation (2) (Cao *et al.*, 2004; Xiao *et al.*, 2010). In a conservative form of momentum equation [Equation (1)], a source term on the right side originates from the mass sediment conservation [Equation (2)]. Introduced erosion and deposition fluxes will be modelled through the sediment transport model.

Sediment transport model

Under the flows with excessively energetic turbulence motions such as dam-break flows, the most governing mechanism of sediment transport is known to be the local entrainment of bed sediments, and thus the non-capacity model can be properly chosen over the capacity model for determining sediment transport (e.g. Capart and Young, 1998; Fraccarollo and Capart, 2002; Cao *et al.*, 2004). The non-capacity model, which is irrelevant to defining sediment transport capacity, describes the sediment exchange process between the water column and the bed in terms of erosion and deposition fluxes. The present study adopts the non-capacity model, which deals with the total sediment loads in a single mode (Cao *et al.*, 2004). Under the long-wave assumption, a depth-averaged sediment transport model can be established to calculate the distribution of sediment caused by the flow field (e.g. Kobayashi and Johnson, 2001; Shimonozo *et al.*, 2007). The resultant depth-integrated sediment transport equation is expressed as

$$\frac{\partial H\overline{c}}{\partial t}+\frac{\partial H\overline{c}\,\widehat{u}_i}{\partial x_i}=\frac{\partial}{\partial x_i}\left(K_h H\frac{\partial \overline{c}}{\partial x_i}\right)+e-d \tag{3}$$

where $\overline{c}$ is the depth-averaged sediment concentration and K_h is the sediment diffusion coefficient in the horizontal plane. It should be mentioned that $\overline{c}$ is a non-dimensional quantity according to its definition, $\overline{c}=(\rho-\rho_w)/(\rho_s-\rho_w)$, in which ρ_w, ρ_s, and ρ denote densities of water, sediment, and sediment–water mixture, respectively. K_h is assumed to be the same as the flow eddy viscosity in this study (see Rakha *et al.*, 1997). Sediments entrained by the flow field are governed by the transport model above. This model is typical for scalar transport, except for additional source and sink terms on the right side, which explain the production and accumulation of sediments through the erosion and deposition processes, respectively. In this study, erosion and deposition fluxes are estimated by empirical formulas, as we will show later. Note that the non-erodible area can be selectively considered by enforcing both e and d to be zero in the model.

Morphodynamic model

The bathymetric changes caused by the divergence of sediment fluxes are calculated by Equation (3). An issue may arise when determining how frequently hydrodynamic and morphodynamic models communicate with each other (Roelvink, 2006). The computationally intensive part of our approach is solving the scalar transport equation for depth-averaged sediment concentration. Once we have the depth-averaged concentration for a given time step, calculating the erosion and deposition fluxes using empirical relations [e.g. Equations (14)–(17)] is very fast. Likewise, updating the bathymetry by the first-order differential equation [i.e. Equation (3)] using these fluxes, which is evaluated by Euler's method, is also computationally very efficient. Therefore, due to these facts, it is anticipated that a noticeable increase in computational performance by reducing the frequency of bathymetry updates cannot be gained. Moreover, it is known that bathymetric changes by short-term events such as storms and tsunamis tend to be relatively fast, while those by long-term events are slow (Shi *et al.*, 2015). Therefore, in the present study, which focuses on tsunami-caused morphological changes, the bathymetry will be updated every time step for use in the Boussinesq and sediment transport models:

$$\frac{\partial h}{\partial t}=\frac{e-d}{1-p} \tag{4}$$

Closures

Since each of the sub-models still have 'open' terms, deterministic evaluations are required during model calculation. Either theoretical or empirical formulas will be applied for those closures.

Bed friction

For turbulent, shallow flows, shear stress at the bottom boundary is often estimated by the quadratic equation

$$\tau_i^b=C_f\rho\overline{u}_i\sqrt{\overline{u}_j\overline{u}_j} \tag{5}$$

where the friction coefficient C_f can be approximated by Manning's formula as (e.g. Geist *et al.*, 2009; Kim and Lee, 2012; Kim, 2015)

$$C_f=\frac{gn^2}{h^{1/3}} \tag{6}$$

In the above equation, n represents Manning's roughness coefficient.

Bottom-induced turbulent eddy-viscosity model

In a situation where bottom friction affects fluid motion, small- to large-scale coherent structures are generated and develop to

be 3D (or at least quasi-3D). In shallow flows, turbulence driven by transverse shear is characterized as large-scale vertical eddies, while turbulence formed by bed friction is associated with small-scale horizontal eddies (Sukhodolov and Rhoads, 2001). Therefore, eddies in vertical and horizontal planes will be modelled through different closures.

Turbulent eddies larger than the grid size are directly computed through the simulation, while those smaller than the grid size (so-called sub-grid-scale eddies) must be modelled using an appropriate turbulence model. For horizontal eddy viscosity, Smagorinsky's turbulent eddy-viscosity model is utilized as

$$v_t^h = (C_s \Delta x_i)^2 \sqrt{2\mathcal{S}_{ij}\mathcal{S}_{ij}} \tag{7}$$

in which C_s is set to 0.2 according to Chen *et al*. (1999), Δx_i is grid size, and $\mathcal{S}_{ij} = \frac{1}{2}\left(\partial\widehat{u}_i/\partial x_j + \partial\widehat{u}_j/\partial x_i\right)$ is a strain-rate tensor on the *ij* plane.

Elder's model, in contrast, is adopted for vertical eddy viscosity as

$$v_t^v = C_h H u^b \tag{8}$$

in which $C_h = \kappa/6$ is used as in Elder (1959) and von Karman's constant, κ, is set to 0.4 in this study. In addition, u^b refers to frictional velocity, which is obtained as $\sqrt{C_f \widehat{u}_i \widehat{u}_i}$.

Turbulence backscattering model

Turbulence energy transferring from sub-grid scales to resolved scales (i.e. backscattering) is particularly significant in a region where high internal shear stresses are present (e.g. the boundary layer) and is not appropriately accounted for in the two horizonzontal dimension (2HD) model through a sub-grid-scale turbulence closure. To better represent 3D turbulence in a 2HD model, a stochastic backscattering model proposed by Hinterberger *et al*. (2007) is included in the momentum equation

$$F_i = C_b \frac{\sqrt{\widehat{u}_j \widehat{u}_j}}{H} \sqrt{\frac{v\sqrt{C_f}}{\Delta t}} r_i \tag{9}$$

where C_b is a constant, v is kinematic viscosity of fluid, Δt is the time increment, and r_i is a random number having unit variance and zero mean. Thus, F_i adds random force to the momentum equation, being responsible for the stochastic backscattering of turbulence energy from sub-grid to resolved scales.

Eddy-viscosity-based wave-breaking model

The physical process of wave breaking is often conceptualized through an eddy-viscosity model. This kind of model presumes that, when waves break, large amounts of wave energy are transformed into turbulent kinetic energy and eventually dissipate. This idea introduces an additional term, R_i, in the momentum equation in order to reflect the energy dissipation through wave breaking (Kennedy *et al*., 2000)

$$R_i = \frac{1}{H}\left[\frac{(1+\delta_{ij})}{2}\frac{\partial}{\partial x_j}\left\{v_b \frac{\partial(H\widehat{u}_i)}{\partial x_j}\right\} + \frac{|\epsilon_{ij}|}{2}\frac{\partial}{\partial x_j}\left\{v_b \frac{\partial(H\widehat{u}_j)}{\partial x_i}\right\}\right] \tag{10}$$

where δ_{ij} is the Kronecker delta function and ϵ_{ij} the Levi-Civita symbol of rank 2 (Tyldesley, 1973).

The eddy viscosity introduced by wave breaking is calculated as

$$v_b = B l_b^2 H \zeta_t \tag{11}$$

where l_b(=1.2) is a mixing-length coefficient and subscript t is the time derivative. Coefficient B, which has a value between 0 and 1, is given by

$$B = \begin{cases} 1 & \zeta_t \geq 2\zeta_t^* \\ \dfrac{\zeta_t}{\zeta_t^*} & \zeta_t^* < \zeta_t \leq 2\zeta_t^* \\ 0 & \zeta_t \leq \zeta_t^* \end{cases} \tag{12}$$

The parameter ζ_t^* is also determined by

$$\zeta_t^* = \begin{cases} \zeta_t^F & t \geq T^* \\ \zeta_t^I + \dfrac{t - t_0}{T^*}\left(\zeta_t^F - \zeta_t^I\right) & 0 \leq t - t_0 < T^* \end{cases} \tag{13}$$

where t_0 denotes the time of breaking initiation and $T^*\left(=5\sqrt{h/g}\right)$ is the transition time. ζ_t^I and ζ_t^F are initial and final values of ζ_t^* during the breaking process, and are set to $0.65\sqrt{gh}$ and $0.15\sqrt{gh}$, respectively, in the present study. Theoretical backgrounds and verifications of the wave-breaking model can be found in Kennedy *et al*. (2000).

Erosion flux

Sediment exchanges between a sediment boundary layer and flow fields are estimated through erosion and deposition fluxes. Various types of formulas have been developed for erosion and deposition estimates under either steady or unsteady flows and are mostly based on experimental data (see e.g. Castro Díaz *et al*., 2008; Abderrezzak and Paquier, 2011). Among these, an empirical formula proposed by Cao *et al*. (2004) is adopted in the present model equations and has shown successful predictions over shallow flows in recent studies (e.g. Kim and Lee, 2012).

The erosion flux, e, can be obtained by

$$e = \begin{cases} \varphi(\theta - \theta_c)(\bar{u}_i \bar{u}_i)^{0.5} H^{-1} (D_{50})^{-0.2} & \text{if } \theta \geq \theta_c \\ 0 & \text{else} \end{cases} \tag{14}$$

in which φ is the dimensional empirical parameter ($m^{1.2}$), θ is the Shields parameter, θ_c is the critical Shields parameter, and D_{50} is the median grain diameter of the sediment. Here the Shields parameter is defined as

$$\theta = \frac{\left(u^b\right)^2}{(\rho_s/\rho_w - 1) g D_{50}} \tag{15}$$

where ρ_s and ρ_w are the density of sediment and fluid, respectively.

It should be mentioned in light of the erosion model [i.e. Equation (14)] that an erosion flux is linearly dependent on the free parameter φ; so the higher the value of φ, the more severe the erosion. Geomorphologically speaking, a larger value of φ represents more erosion-sensitive conditions, and vice versa. A typical value of φ is not so well-defined, but ranges empirically from $O(10^{-6})$ to $O(10^{-2})$ depending on the hydrodynamic and geometric conditions. The final determination of φ can be made through a calibration process (see Cao *et al*., 2004; Kim and Lee, 2012). Even with this general guidance, calibration focusing on this parameter necessarily requires to be carried out for the better selection of the value, and thus will be performed in a later section. The critical Shields parameter

θ_c is another free controller of the erosion model, estimated to be 0.045 according to the preceding studies.

Deposition flux

The deposition flux, d, can be modelled by the following formula (Wu and Wang, 2007):

$$d = \alpha \bar{c} w_0 \tag{16}$$

where $\alpha = \min[2, (1-p)/\bar{c}]$. The fall velocity w_0, unless otherwise specified, is estimated from (Ponce, 1989)

$$w_0 = \left\{ \frac{4}{3} \frac{gD_{50}}{0.2} (\rho_s/\rho_w - 1) \right\}^{0.5} \tag{17}$$

Calculation procedure of the model

Following the procedure proposed by Karambas and Koutitas (2002) and Rakha *et al.* (1997), the full calculation process can be described as given below. Assuming that all dependent variables $(\zeta, \hat{u}, \hat{v}, h, \bar{c}, d, e)$ in the Boussinesq model, sediment transport model, and morphodynamic model at $t = t_n$ are known:

1. Calculate free surface and velocity values at $t = t_{n+1}$ by processing the predictor step in the Boussinesq model.
2. Perform the implicit corrector step in the Boussinesq model to obtain free surface and velocity values at $t = t_{n+1}$ and compare them with the predictor-step values. Iterate this step until all the relative errors between predictor and corrector steps are less than the given value of 10^{-4}.
3. Transfer free surface and velocity information at $t = t_n$ and at $t = t_{n+1}$ into the sediment transport model to calculate sediment erosion and deposition fluxes at each time step.
4. Using the predicted sediment fluxes in the sediment transport model, estimate sediment concentration at $t = t_{n+1}$.
5. Perform a corrector step in the sediment transport model to assess sediment concentration at $t = t_{n+1}$. Repeat this step as in the Boussinesq model.
6. Calculate the new bathymetry at $t = t^{n+1}$ using the morphodynamic model.
7. Transfer the bathymetry information at $t = t^{n+1}$ into the Boussinesq model for the next time step.
8. Update all dependent variables in the model.
9. Return to step 1 for the next time step.

This procedure in the integrated model is schematized in Figure 1, showing that the Boussinesq model, sediment transport model, and morphodynamic model are all systematically connected to communicate mutually.

Numerical Methods

For arbitrary bottom profiles and boundary conditions, model equations can be solved numerically. In the Boussinesq and sediment transport model equations, a finite-volume method is adopted for spatial derivatives, while the third-order Adams–Bashforth predictor and the fourth-order Adams–Moulton corrector scheme are used for time derivatives (Wei *et al.*, 1995; Kim *et al.*, 2009). The well-known issue arising from incomplete conservativeness due to the bottom slope term in the Boussinesq model is accommodated by employing the surface gradient method introduced by Zhou *et al.* (2001). This preserves the conservative property of the mass and momentum equations. More details on the numerical scheme are presented in the Supporting Information.

Test Cases

To validate the developed model, four problems involving sediment processes were tested. The time step can be set to change dynamically based on the Courant number, which was found to be stable up to 0.5 (Kim *et al.*, 2009; Son *et al.*, 2011). Meanwhile, an initial value of the Courant number was set differently in each simulation, according to the previous application.

Case 1. One-dimensional dam break

One-dimensional dam-break flow over a movable bed was simulated by the model, and the computed results were compared with laboratory data reported by Fraccarollo and Capart (2002). This problem concerns bottom change caused by sudden erosional dam-break flows over a loose sediment bed and has been addressed in other studies (Wu and Wang, 2007, 2008; Kim and Lee, 2012).

The experiment was performed in a channel of 2.5 m length, 0.1 m width, 0.25 m depth, with a 0.1-m initial water depth upstream and dry conditions downstream. Cylindrical-shaped PVC particles having 3.5 mm spherical-equivalent diameter and 1540 kg m^{-3} density were used as movable bed materials. Even though the particle size falls into very fine gravel, it is found to be applicable without special treatment to the sediment model, which is based on shallow water or Boussinesq equations through similar studies (Wu and Wang, 2007, 2008; Kim and Lee, 2012). The dam-break waves were generated by abruptly removing a slice gate between upstream and downstream regions. The subsequent flow caused severe bed erosion as shock waves moved downstream.

In the numerical simulation, the grid size (Δx) was 0.005 m and the time step (Δt) was dynamically determined by the Courant number of 0.1. The sediment porosity (p) and settling velocity (w_0) were set to 0.3 and 0.18 m s^{-1}, respectively, based on Wu and Wang (2008). The Manning coefficient (n) was 0.025 and the empirical coefficient (φ) was 0.003. Such a setting was guided by Kim and Lee (2012); examining in depth the sensitivity of different parametric settings and consequently pointing out a careful choice of empirical parameters in the numerical model will result in good predictions. Therefore, the above values were selected after calibration tests.

Simulated snapshots of free surface elevations and bed profiles at different time steps were compared with measured data (Figure 2), and relatively good agreement between calculation and measurement was found. The eroded beds and hydraulic jump locations were successfully predicted by the present model, although some discrepancies existed in surface elevations near the leading front and hydraulic jump locations. Similar errors can be found in related literature (Wu and Wang, 2007, 2008; Kim and Lee, 2012), and it may be inferred that some errors can be caused by idealizing sediment particle shapes from cylinder to sphere. It should also be noted that sediment erosion existed mostly in suspension, similar to Kim and Lee's (2012) results, and thereby erosion only occurred without deposition in Figure 2.

For different values of the empirical coefficient (φ) varying from 3×10^{-5} to 3×10^{-2}, a sensitivity analysis was also performed. Figure 3 compares surface elevations, bottom profiles, depth-averaged velocities, and concentrations calculated

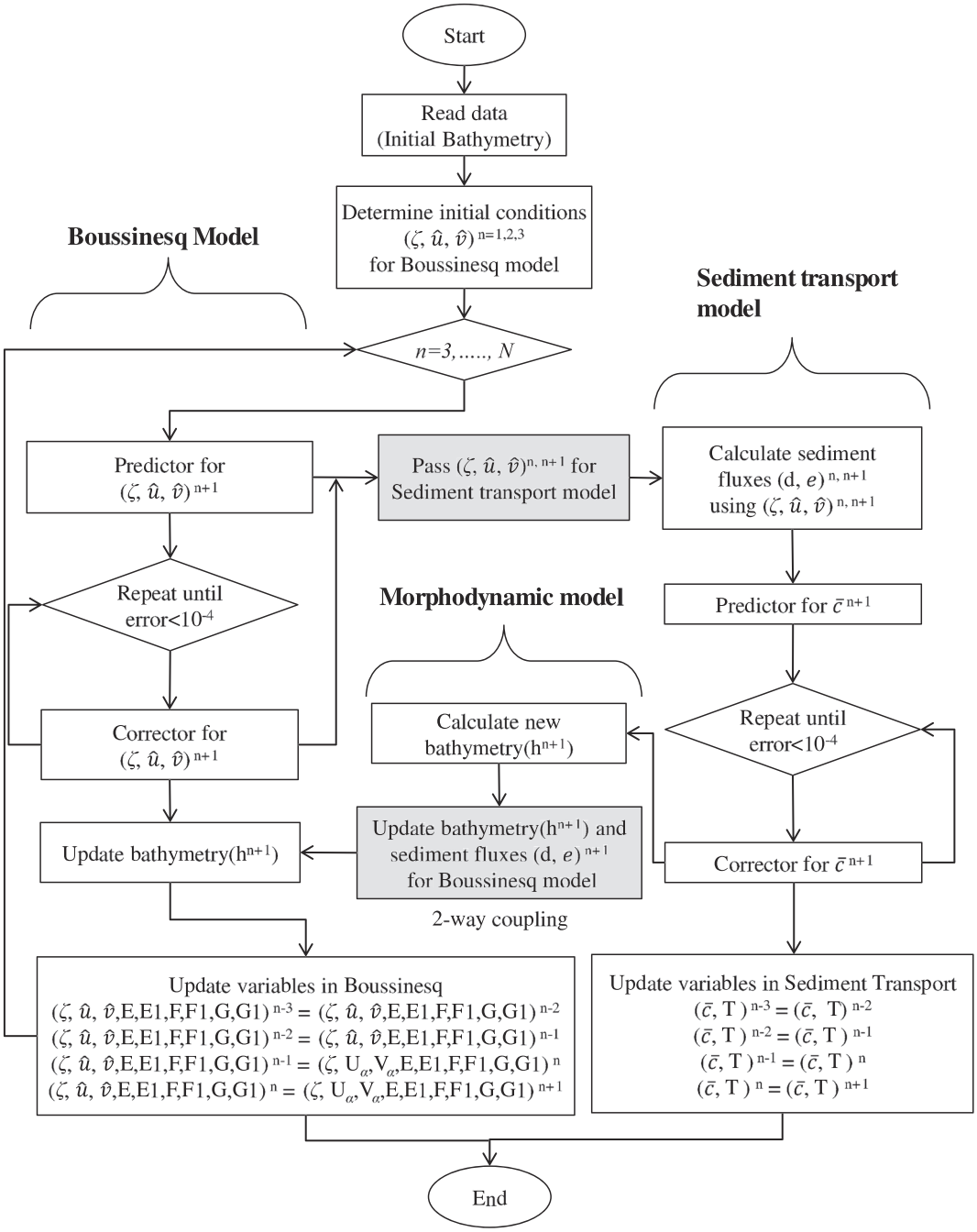

Figure 1. Flowchart of computational procedures in the integrated model.

for different φ. Depending on the value of φ, computation results with large variations in both surface hydrodynamics and landforms were yielded. It is obvious that the higher φ, the deeper and wider the eroded bed formed. Accordingly, the severe level of erosional process affected water surface propagation in such a way that the surface wave interacts more actively with the bed, resulting in higher concentration and retarded wave propagation with a reduced velocity and an increased surface level at front. This implies that a highly erosive condition can be taken into account by selecting a large φ, which is in turn associated with surface hydrodynamics. Therefore, determination of the proper φ is required to be made under the consideration not only of morphologic condition, but also hydrodynamic condition. Since this laboratory-scale case has a bed material with relatively low specific gravity, a relatively high φ of $O(10^{-3})$ is shown to be appropriate.

Case 2. One-dimensional finite train of breaking solitary waves

Kobayashi and Lawrence (2004) carried out laboratory experiments in a wave flume (L 30 m, W 2.4 m, H 1.5 m) to study beach profile changes under breaking solitary waves, as illustrated in Figure 4. A solitary wave of 0.216 m height was generated by a wave paddle at the left end of the flume and propagated to the sloping beach composed of sand grains. The beach had an initial slope of 1/12 and was expected to change due to the impact of breaking solitary waves. This process was repeated eight times to consider the effect of multiple wave attacks. Bottom profiles after four and eight wave attacks and surface elevations at eight locations after four wave attacks were measured. The median grain diameter (D_{50}), fall velocity (w_0), specific gravity, and porosity (p) were 0.18 mm, 2.0 cm s^{-1}, 2.6, and 0.4, respectively.

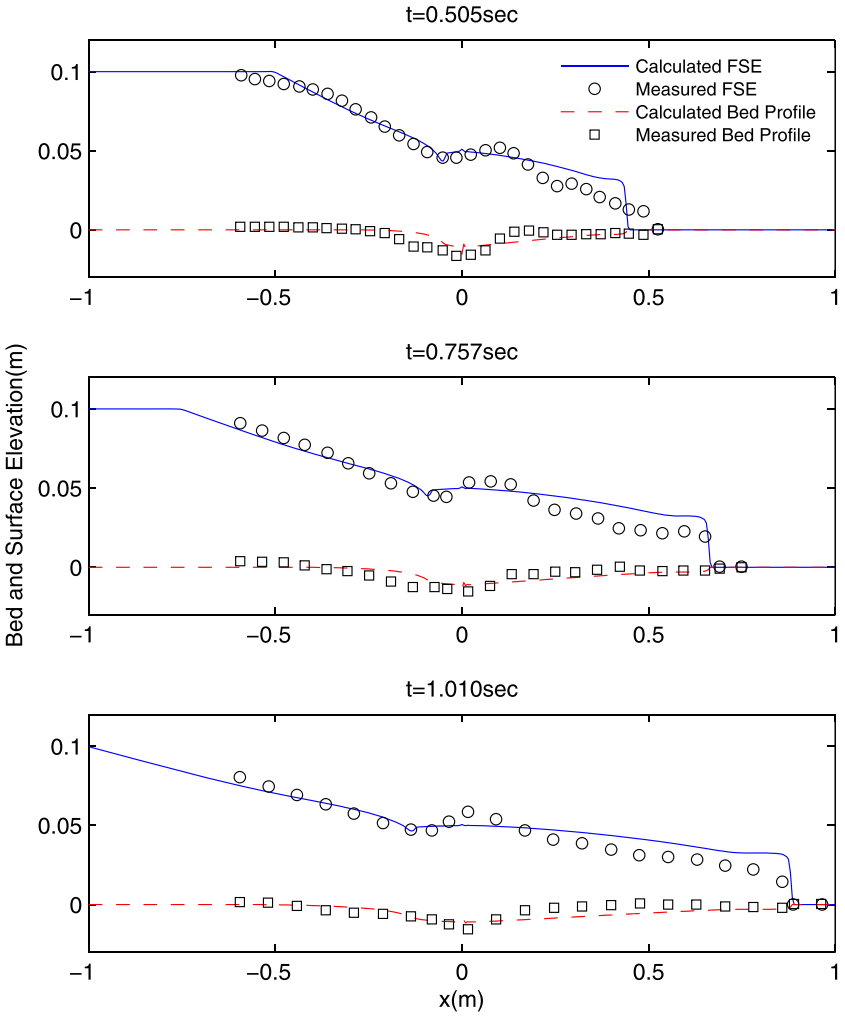

Figure 2. Calculated free surfaces (solid line) and bed elevations (dashed line) of dam-break flows over a movable bed at different time steps. Measured free surfaces (circle) and bed elevations (square) are from Fraccarollo and Capart (2002). [Colour figure can be viewed at wileyonlinelibrary.com]

To evaluate the accuracy and performance of the numerical model, we recreated the above experiment using the same conditions. The simulation was performed using a uniform grid size of 0.1 m and varying the time step by the Courant number of 0.4. For Manning coefficient (n) and empirical parameter (φ), 0.025 and 7.5×10^{-6} were determined after calibration. Such a smaller value of φ (i.e. less erosive) is most likely attributable to weakened shear stress at the bed, which originates from wave-breaking-induced energy dissipation. The eddy-viscosity model proposed by Kennedy *et al.* (2000) was used so as to account for the turbulent mixing and dissipation caused by wave breaking, which affects bed-shear stress.

In Figure 5, calculated surface elevations at different time stages are given with measured data. Calculated results agreed well with measured ones, while some errors were seen in gauges 7 and 8 for measuring wave runup and rundown. Calculated beach profiles compared with measured data are given in Figure 6. Fairly good agreement was found in the results of both four and eight wave breaks. A significant erosion process at the foreshore was observed in measured and computed results, which may be explained by the strong backwash current initiated when a solitary wave retreats. The entrained sediments were deposited on the seaward side with the help of flow advection. In addition, the discrepancy in gauges 7 and 8 in Figure 5 occurring overland is mostly due to the relatively inaccurate prediction of water depth near the shoreline (Figure 6). The overall trends in evolution of deposition and erosion are compared with measured data in terms of normalized maximum deposition and erosion depth, as shown in the lower plot of Figure 6. The continuous increase in erosion and deposition depth were observed during successive wave attacks, both in measured and calculated results. Such increases were approximated to be 0.06H per single wave (Kobayashi and Lawrence, 2004).

There are two possible causes of the discrepancy between the experimental and numerical data. As shown in Figure 5, the surface elevation in the swash zone is overestimated and thus, the computed sediment transport is correspondingly expected to produce some errors between numerical and experimental results. Another reason may be the seepage force acting on the measurement in the experiment. In the laboratory experiment, the sediment at the seabed was supposed to experience upward-directed pressure gradient force, as high as almost 30% of the submerged weight of the sediment (Li *et al.*, 2019). This seepage-force factor is not well considered in the present model, even though it can influence the sediment process.

Additionally, the inclusion of a wave-breaking model is also tested to examine its effect on the bottom change. Figure 7 describes calculated beach profiles with and without the wave-breaking model. Even though both cases yield almost identical results in terms of bottom profile changes, the case with the wave-breaking model predicts deeper erosion. Such a slight difference is likely to originate from the decreased bed stress due to wave breaking.

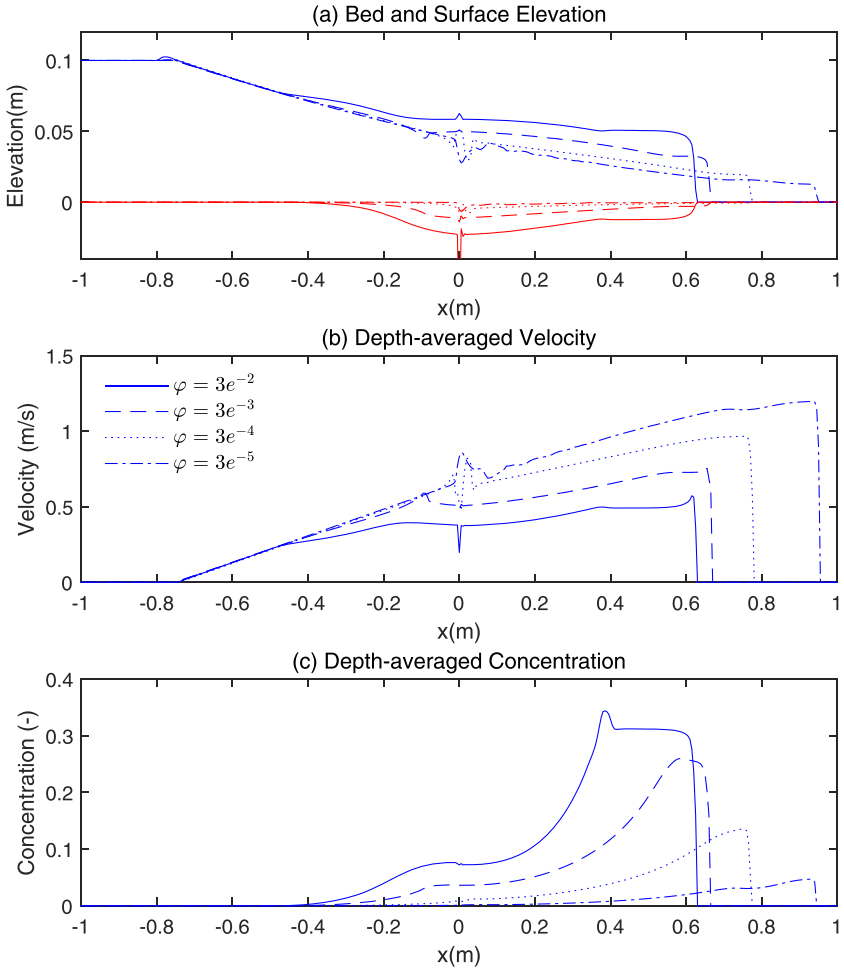

Figure 3. Calculated results with different φ at $t = 0.757$ s: (a) free surfaces (blue lines) and bed elevations (red lines); (b) depth-averaged velocity; (c) depth-averaged concentration. [Colour figure can be viewed at wileyonlinelibrary.com]

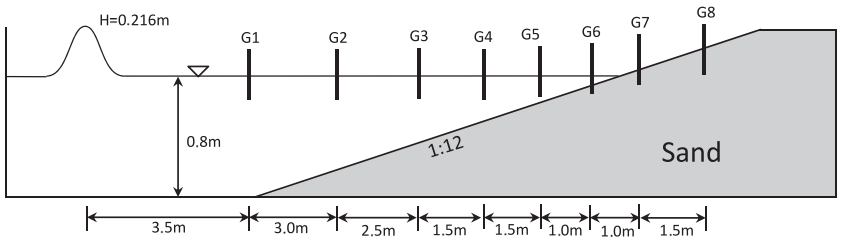

Figure 4. Experimental setup for breaking solitary waves on a sloping beach.

Case 3. Two-dimensional dam-break flow through a partial breach over a movable bed

The model was tested using a partially breached dam-break flow case, conducted experimentally by Xia *et al.* (2010). The experiment was performed in a channel of 18.5 m length and 1.6 m width, with a movable bed section of coal ash along the centre (Figure 8). The median diameter (D_{50}) of the coal ash was 0.135 mm and the density was 2248 kg m^{-3}. Initial upstream and downstream water depths were 0.4 and 0.12 m, respectively. Once the thin-walled dam located at X = 2 m was removed, strong, jet-like flow through a 0.2 m-wide gap was generated, causing significant erosion around the gap. Cross-sectional profiles of the bottom were measured at CS1 (X = 2.5 m) and CS2 (X = 3.5 m) after 20 s using an ultra-acoustic topographic surveying meter.

The physical results of the experiment were reproduced numerically in the model with a grid resolution of 0.025 m. As in the previous tests, the time step was varying, with the Courant number set to 0.3. Following Xia *et al.* (2010), the Manning coefficient (n) was determined as 0.015, while the empirical parameter (φ) was tuned to 5.0×10^{-5} (Kim and Lee, 2012). The fall velocity, which had not been given in the experimental conditions, was approximated using Equation (17).

Figure 9 shows the differences in bottom profile between the simulated and measured data. The BSS (Brier skill score; van Rijn *et al.*, 2003) of the numerical results without turbulent eddy viscosities (v_t^h, v_t^v) and the BSM (backscattering model) at CS1 is calculated as 0.75, which indicates good agreement based on van Rijn *et al.* (2003), while the case considering both v_t^h and v_t^v produced excellent agreement, having BSS = 0.80. The primary cause of this difference lies in the fact that disregarding turbulent eddy viscosity leads to insufficient description of the energy dissipation process through it, which consequently forms more rapid flow with deeper bottom

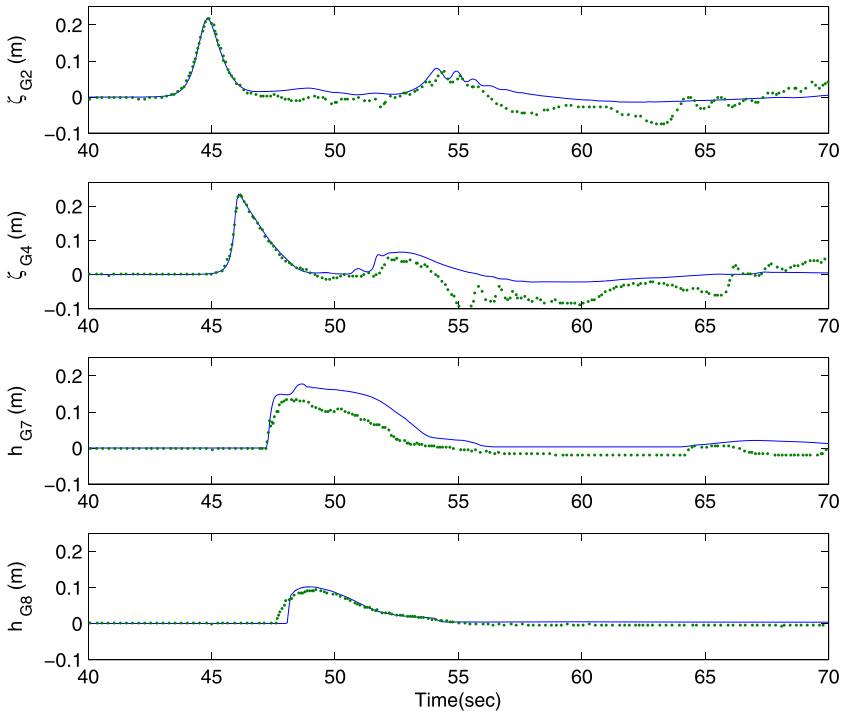

Figure 5. Measured (dotted line) and calculated (solid line) surface elevations caused by breaking solitary waves on a sloping beach. [Colour figure can be viewed at wileyonlinelibrary.com]

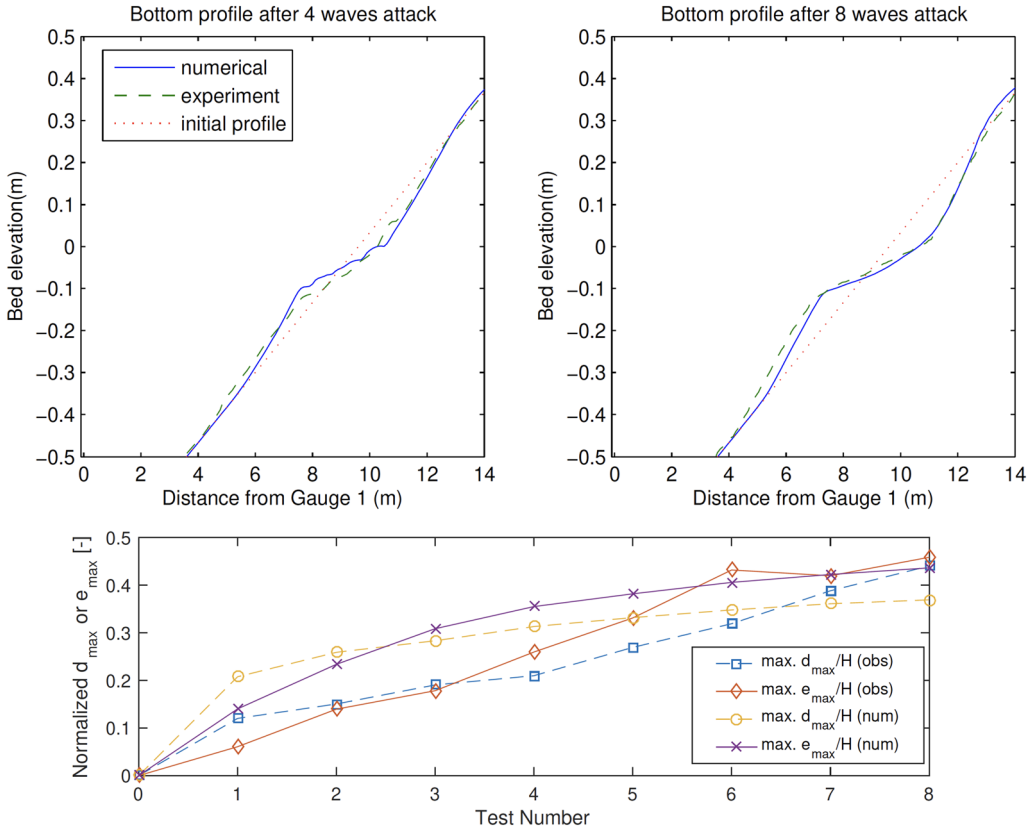

Figure 6. Upper panel: Measured and calculated beach profiles caused by breaking solitary waves on a sloping beach. Lower panel: Observed and numerical maximum deposition and erosion depth for every repetition. [Colour figure can be viewed at wileyonlinelibrary.com]

erosion. Therefore, reasonable agreement was found in both CS1 and CS2 when including turbulence effects, while the calculations (solid dotted lines) overestimated the peak erosion depth at CS1. Addressing this issue, Xia *et al.* (2010) indicated that simply using the turbulence closure model is not sufficient to generate the horizontal circulation rapidly formed by jet-like flows, resulting in errors. This point of view was shared by Kim and Lee (2012), who indicated that the use of turbulence closure that is insufficient to model the rapid mixing by the strong jet flows occurring around the side wall and corner can produce errors. In addition, the non-uniformity of bed material in the experiment and expected armoring effects are thought to

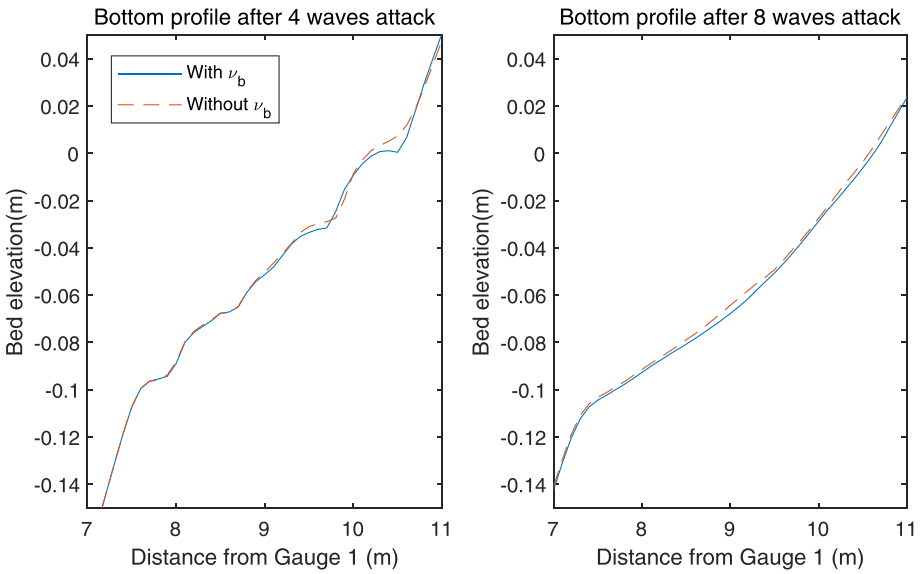

Figure 7. Calculated beach profiles (solid, with a wave-breaking model; dashed, without a wave-breaking model). [Colour figure can be viewed at wileyonlinelibrary.com]

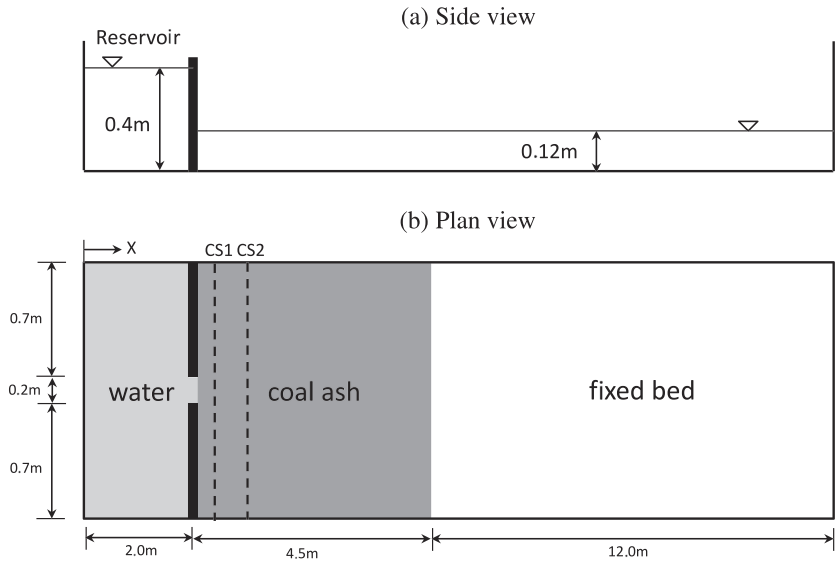

Figure 8. Experimental setup of a dam-break flow through a partial breach over a movable bed.

be responsible for the mismatch between modelled results and experimental data. By considering the energy exchange involved in such processes, the results (solid lines) in Figure 9 can be improved.

As pointed out by Hinterberger *et al.* (2007), in depth-averaged 2D modelling, turbulence backscattering needs to be considered in the presence of strong horizontal shear (as near the breached gap in this test). Turbulence energy transfer from the unresolved sub-grid scale to the resolved 2D flows can be explained using a turbulent backscattering model. The dashed lines in Figure 9 represent the same results as the solid lines, but including the backscattering model. Consequently, when considering turbulent eddy viscosity, the BSS value increases 7%, while adding a turbulent BSM makes it even more precise up to 0.87. These results demonstrate that the prediction of peak erosion depth at CS1 is improved when considering turbulence backscattering effects.

Under this numerical configuration, the parametric sensitivity of φ to the numerical result was examined as in Case 1. A total of five different φ values were tested and the results were compared, as shown in Figure 10. As in the previous case, a bigger φ value promoted a more active erosion process, resulting in the maximum erosion depth changing with an approximate order of magnitude of $O(\Delta h) \sim O(\log(\Delta\varphi))$ and also revealing that the selection of φ in $O(10^{-5})$ is desired for the proper consideration of morphodynamic changes of sediment particles having a specific gravity of 2.25.

Case 4. Two-dimensional dam-break flow in a movable bed channel with a sudden increase in width

The final test of the model is dam-break flow over a movable bed channel with a sudden increase in width. Goutiere *et al.* (2012) carried out an experiment on this case using a varying-width flume at the Hydraulics Laboratory of Université Catholique de Louvain, Belgium. The flume was 6 m long, 0.25 m wide upstream, and 0.5 m wide downstream (Figure 11). A temporal dam was installed at $X = 3$ m, 1 m upstream of the sudden enlargement, and was removed quickly, downward,

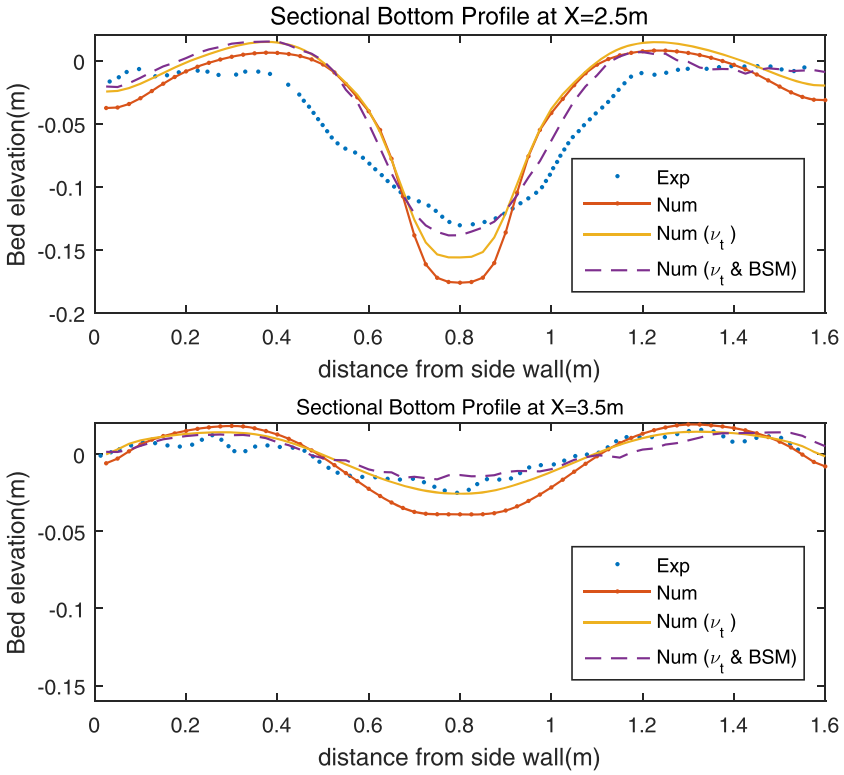

Figure 9. Measured and calculated bottom profiles of a dam-break flow through a partial breach over a movable bed: experimental record (dotted), numerical solution without v_t (solid dot), numerical solution with v_t (solid), numerical solution with v_t and backscatter model (dashed). [Colour figure can be viewed at wileyonlinelibrary.com]

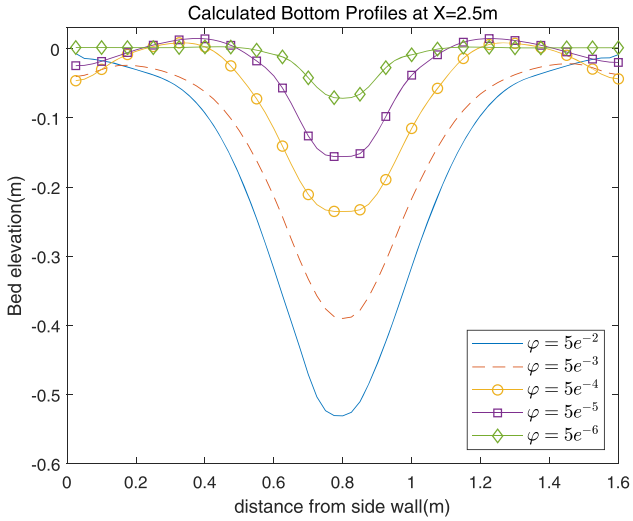

Figure 10. Calculated bottom profiles with various φ. [Colour figure can be viewed at wileyonlinelibrary.com]

to generate dam-break waves. A movable bed was layered 0.1 m thick with coarse sand grains (median diameter D_{50} and specific gravity of 1.82 mm and 2.68, respectively) in the flume and fully saturated. The initial water depth upstream was 0.25 m and the downstream area was dry. Surface elevations were measured using ultrasonic gauges at eight different locations (Figure 11) during the test. Laser sheet imaging was used to measure bottom profiles after the experiment.

For the numerical simulation, the computational domain was formed using a uniform grid size ($\Delta x = \Delta y = 0.01$ m). A free-slip boundary condition was imposed on all domain sides, based on the glass side walls of the flume. Not given by Goutiere *et al.* (2012) in the experimental conditions, the fall velocity was approximated using Equation (17), as in the previous case. The Manning coefficient (n) and empirical parameter (φ) were equal to 0.025 (Xia *et al.*, 2010) and 5.0×10^{-5} (Kim and Lee, 2012), respectively.

Figure 12 compares calculated and measured surface elevations at gauges U1–U7, and the overall agreement is good. Figure 13 shows the comparison of bed topography between computed and observed data after 20 s. In particular, bed levels calculated by 3D hydraulic models in Marsooli and Wu (2014) were included to investigate the validity of the use of the Boussinesq model. Throughout four different locations, general trends of erosion and deposition were effectively predicted by both models. Based on direct comparison between the two model results, the adequacy of the Boussinesq model in accounting for 3D features of dam-break flows can be inferred. Boussinesq model results predicted well the erosion depth over all locations, while the 3D model underestimated at X = 4.15 m. In contrast, the calculation of deposition was less accurate in both model results, specifically at X = 4.05 and 4.15 m. The discrepancy may have resulted from complex hydraulic behaviour near the expansion zone (Marsooli and Wu, 2014) and a relatively shallow depth of the water compared to the size of the bed material (Xia *et al.*, 2010). It is worthwhile noting that this tendency has been reported in similar studies (Xia *et al.*, 2010; Kim and Lee, 2012; Wu *et al.*, 2012; Marsooli and Wu, 2014).

Field-Scale Application; Far-Field 2011 Tohoku-oki Tsunami

The 2011 Tohoku-oki tsunami was chosen as a practical application of the model in an actual coastal region. Far-field tsunami events can lead to severe morphologic changes, especially in the nearshore area (Lacy *et al.*, 2012; Weiss and Bourgeois, 2012; Wilson *et al.*, 2012; Yamashita *et al.*, 2016).

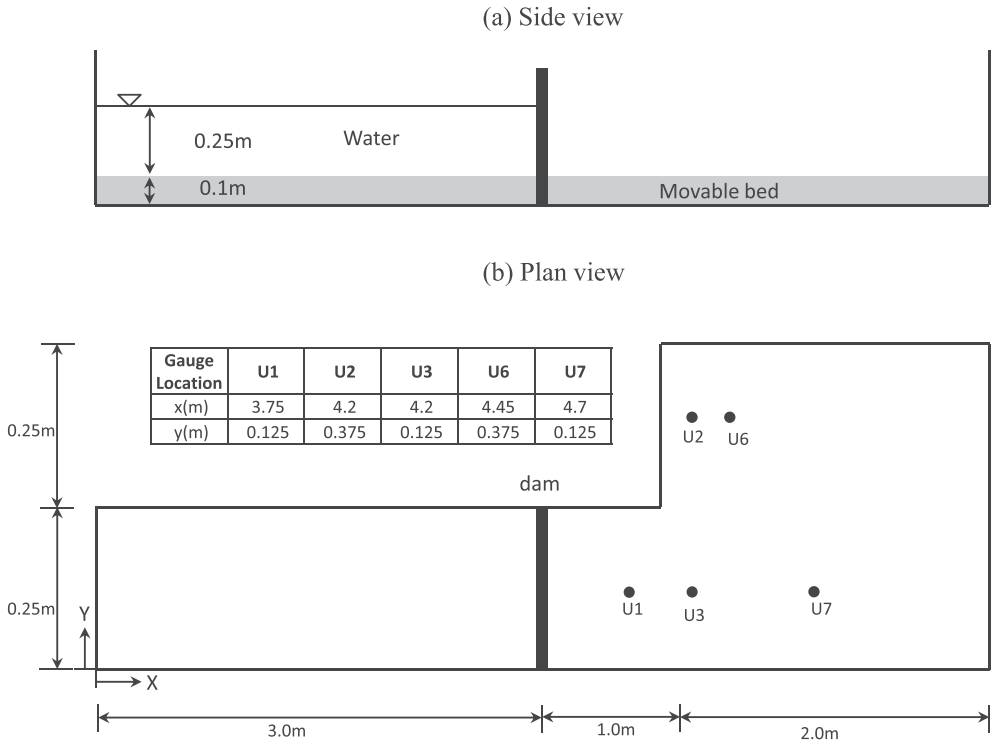

Figure 11. Experimental setup of a dam-break flow in a movable bed channel with a sudden increase in width.

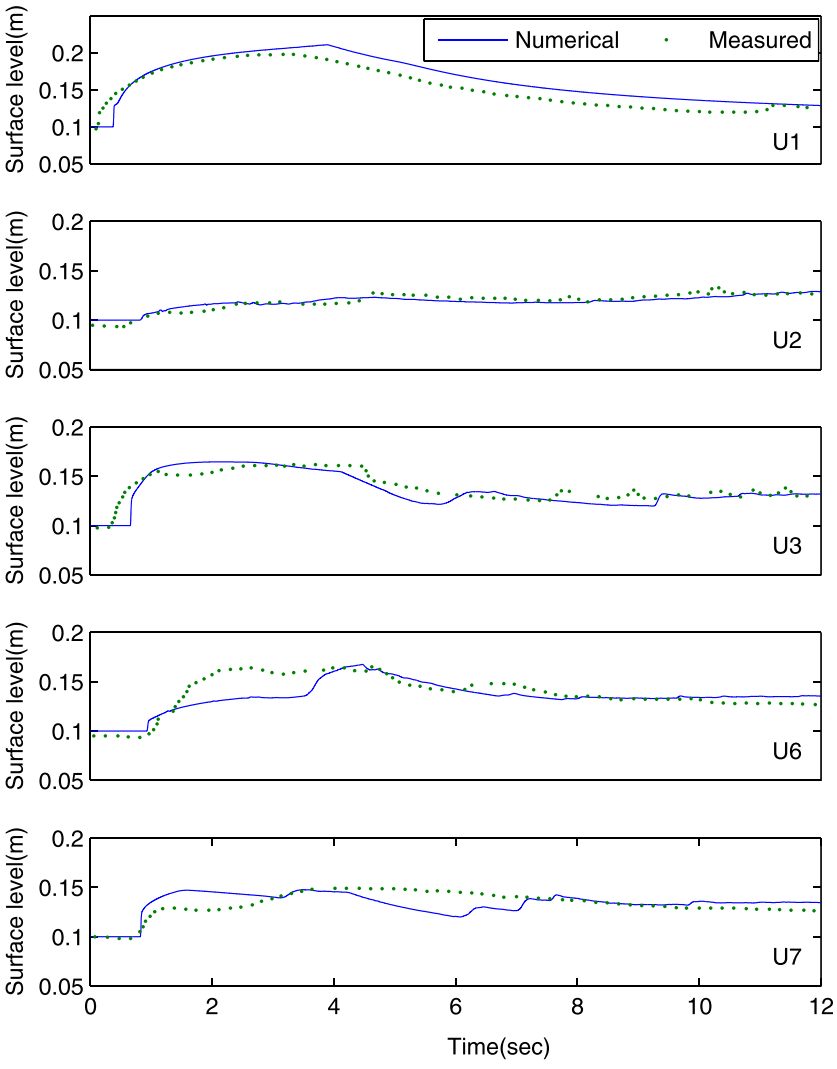

Figure 12. Measured and calculated surface levels at gauges U1 to U7. [Colour figure can be viewed at wileyonlinelibrary.com]

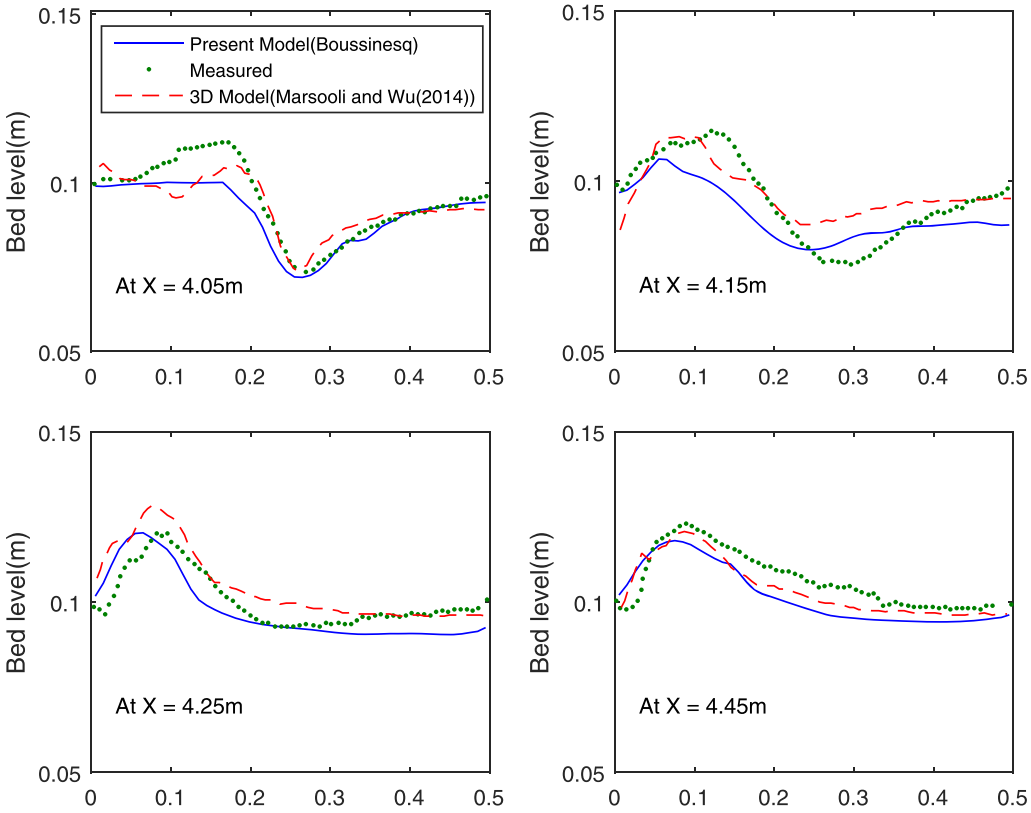

Figure 13. Measured and calculated bottom topography at cross-sections. [Colour figure can be viewed at wileyonlinelibrary.com]

Realizing that relatively small-amplitude tsunami waves [$<O(1 \sim 2$ m)] may create strong current fields near harbour basins (e.g. Son *et al.*, 2011; Lynett *et al.*, 2012; Admire *et al.*, 2014), the model needs to predict tsunami-induced currents as accurately as it does free surface evolutions when estimating morphological changes near the shoreline.

Traditional approaches to measuring sediment transport by tsunami waves are based on the shallow water equation model (e.g. Li *et al.*, 2012). However, due to the complex geometric and hydrodynamic environments in waterfront areas, more dedicated investigations into wave dynamics are required for accurate sediment prediction under 'long-wave' conditions, such as those created by tsunamis and storm surges. In an effort to better estimate the current field generated by far-field tsunami waves in the nearshore area, we employed the multi-grid and multi-physics model developed by Son *et al.* (2011). A total of five nested grids with different grid sizes were used to simulate the Tohoku-oki tsunami. The final grid, focusing either on the Crescent City Harbor area or the Santa Cruz Harbor area, had the smallest domain, with a relatively fine grid size of 9 m. Due to the complex nearshore geophysical configurations, the final grid was solved using the Boussinesq equations, which included higher-order dispersive and turbulent properties (Son *et al.*, 2011). This model was used to represent the viscous effects of bottom shear, and the associated rotationality, on the flow structure.

For direct comparison between Boussinesq and shallow water model outputs, simulations using shallow water equations in the final grid were performed as well. The other grids, which generally covered a larger domain with deeper ocean area instead of shallow coastal regions, were solved using shallow water equations. The initial hydrodynamic condition of the Tohoku-oki tsunami was generated using a finite fault model obtained from the USGS Earthquake Hazard Program (http://earthquake.usgs.gov/) and bathymetry data from NOAA National Geophysical Data Center (see Lynett *et al.*, 2012). The numerical parameters used in these simulations are detailed in Table I.

Simulations were performed for 14 h after the first tsunami wave arrived at the harbour in order to allow enough time for sediment processes; significant further changes in sedimentation were not observed in simulations longer than 14 h. Figure S1 in the Supporting Information shows a snapshot of surface elevations in all grids at t = 878 min since the earthquake. A time series of free surface elevation at the tidal station located at Crescent City Harbor (Station ID 9419750) was compared with simulated elevations, as shown in Figure 14. The predicted water surface elevation is very similar and in good agreement with the measurement, while some errors are found in both phase and amplitude after about five waves. Such a discrepancy occurring after some simulation time is supposed to be an accumulated diffusive error attributed to the limiter used in the finite-volume scheme.

The parametric values used in the sediment simulation were specific gravity = 2.68, p=0.4, n=0.025, and $\varphi = 5 \times 10^{-5}$, which are in acceptable ranges for coastal sedimentation (see e.g. Kim and Lee, 2012). Meanwhile, different D_{50} values covering from 0.15 mm (fine sand) to 0.50 mm (coarse sand) were tested in turn to examine the sensitivity to grain size (e.g. Sutherland *et al.*, 2004). The settling velocity (w_0) was also estimated through Equation (17) and the Courant number of the Boussinesq model was set to 0.4. Bathymetric changes of different D_{50} values and hydrodynamic models at the harbour entrance are shown in Figure 15 (Crescent City Harbor) and Figure 16 (Santa Cruz Harbor) in comparison with observed data.

For the quantitative assessment of modelled results, BSS values from simulations with different D_{50} values and hydrodynamic models were calculated as summarized in Table II. The BSS values for the Boussinesq model are all found to be positive and indicate reasonable accuracy, showing little variation with grain size. As for the variation due to grain size, both erosive

Table I. Grid setup for the 2011 Tohoku-oki tsunami simulation.

Grids	*x* Range (longitude, E)	*y* Range (latitude, N)	*nx* × *ny*	*dx*	*dt* (s)	Model
North Pacific	130°00′00′′ ~ 280°00′00′′	0°00′00′′ ~ 60°00′00′′	4501 × 1801	2′	1	LSW(S)[a]
West Coast	215°00′15′′ ~ 244°59′45′′	30°00′15′′ ~ 49°59′45′′	3600 × 2400	30′′	0.5	LSW(S)
Northern California	235°00′00′′ ~ 236°59′57′′	40°00′00′′ ~ 42°59′57′′	2400 × 3600	3′′	0.25	LSW(S)
Monterey Bay	237°15′00′′ ~ 238°14′57′′	36°15′00′′ ~ 37°14′57′′	1200 × 1200	3′′	0.25	LSW(S)
Crescent City Coast	235°46′12′′ ~ 235°51′36′′	41°42′36′′ ~ 41°46′12′′	972 × 648	9.0 m	0.125	NLSW[b]
Santa Cruz Coast	237°55′45′′ ~ 238°03′00′′	36°54′30′′ ~ 37°00′00′′	1305 × 990	9.0 m	0.125	NLSW
Crescent City Harbor	235°47′51′′ ~ 235°49′33′′	41°43′41′′ ~ 41°45′24′′	309 × 309	9.0 m	0.125	BOUSS[c] or NLSW
Santa Cruz Harbor	237°59′03′′ ~ 238°00′46′′	36°57′15′′ ~ 36°58′58′′	309 × 309	9.0 m	0.125	BOUSS or NLSW

[a]Linear shallow water model in spherical coordinates.
[b]Nonlinear shallow water model in Cartesian coordinates.
[c]Boussinesq model in Cartesian coordinates.

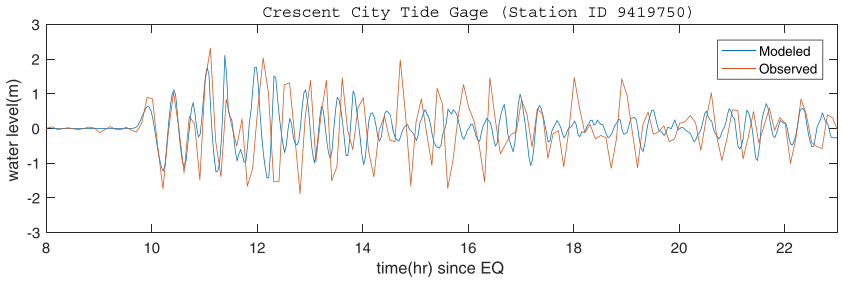

Figure 14. Comparison of water surface elevations from observation (Crescent City Tidal Station, ID 9419750) and calculation. [Colour figure can be viewed at wileyonlinelibrary.com]

and accretive sediment motions are increasingly generated as the grain size reduces. The case of $D_{50} = 0.25$ mm produced the best fit to the observation in both harbours, while increasing the grain size did not improve the model accuracy significantly, as addressed by Sutherland *et al.* (2004). In contrast, the BSS values of the shallow water model in both locations were lower than those of the Boussinesq model, also going negative. In particular, the shallow water BSS values were considered bad in Santa Cruz Harbor. As pointed out in previous tsunami-related studies (Son *et al.*, 2011; Lynett *et al.*, 2012; Borrero *et al.*, 2015), strong, dynamic, and persistent current fields often formed nearshore (Kalligeris *et al.*, 2016) are appropriately modelled through the fully nonlinear and weakly dispersive Boussinesq-type model with at least a higher-order numerical scheme to effectively control dissipation errors. Consequently, the comparison of BSS values from two different hydrodynamic models implies that the inclusion of higher-order terms in a hydrodynamic model may lead to more successful prediction of sedimentation processes, especially when complex hydrodynamic conditions are involved, as in the harbour area.

Even though the BSS values of the Boussinesq model in both locations are reasonable (van Rijn *et al.*, 2003), those for Santa Cruz Harbor present better agreement. This is most likely due to the smaller coverage of observations and the relative simplicity of the harbour geometry, which is directly connected to the relevant hydrodynamic conditions. Moreover, a detailed comparison between measured and calculated changes revealed that the calculated errors were largely concentrated around the inner harbour, where a complicated geometry exists. It should be noted that in 2HD domains, BSS values will be prone to produce exaggerated errors originating from spatial shifting of erosion or deposition locations, since the BSS compares values point-by-point. Therefore, a low BSS in 2HD is known to be typical (e.g. van Dongeren *et al.*, 2013).

Since the empirical parameter φ was found to largely control morphologic processes and their subsequent effects on surface hydrodynamics through the previous modelling cases, a sensitivity test under real-scale conditions was repeated. Figure 17 presents modelling results in which φ was set differently for the $D_{50} = 0.25$ mm case. Comparison of bathymetric changes and maximum currents for different φ confirms a tendency similar to that observed in previous tests; smaller φ produced less erosive bottom changes. It can be inferred that when the tsunami wave propagates over a highly erodible bed (i.e. large φ value), its momentum is damped due to the strong interaction between surface processes and landforms, so the propagation gets retarded. This process can be supported by reduced maximum currents and increased heights in the high φ case, which is consistent with Figure 3. It should also be noted that, under the 2D field scale of 100 m to 1 km, φ up to $O(10^{-5})$ is recommended for robust and accurate computation (values higher than that are found to develop a highly erosive configuration, incurring numerical instability as well as inaccuracy).

In Figure 17, a similarity in spatial pattern is found between morphodynamic changes and maximum currents, even though their magnitudes are different depending on φ. The area eroded by the tsunami currents forms in shallow depths of less than 5 m, where strong currents over 0.5 Froude number occur, while the maximum erosion depth varies with φ. Meanwhile, sediment deposition mainly takes place in deeper depths adjacent to the erosion area, as a result of reduced flow speed. Therefore, varying the value of φ is supposed to change the degree of erosion/deposition and flow speed without significantly changing the spatial pattern of sedimentation.

The detailed process of generation and movement of sediment particles can be inferred by looking at numerical results at specific time levels. For instance, in Crescent City Harbor, current speed, sediment concentration, and erosion/deposition fluxes can be seen in Figure 18. At time t = 637 min since the earthquake, the tsunami rushes out of the harbour basin and very active sedimentation processes occur in the vicinity of the outer and inner harbour entrances, due

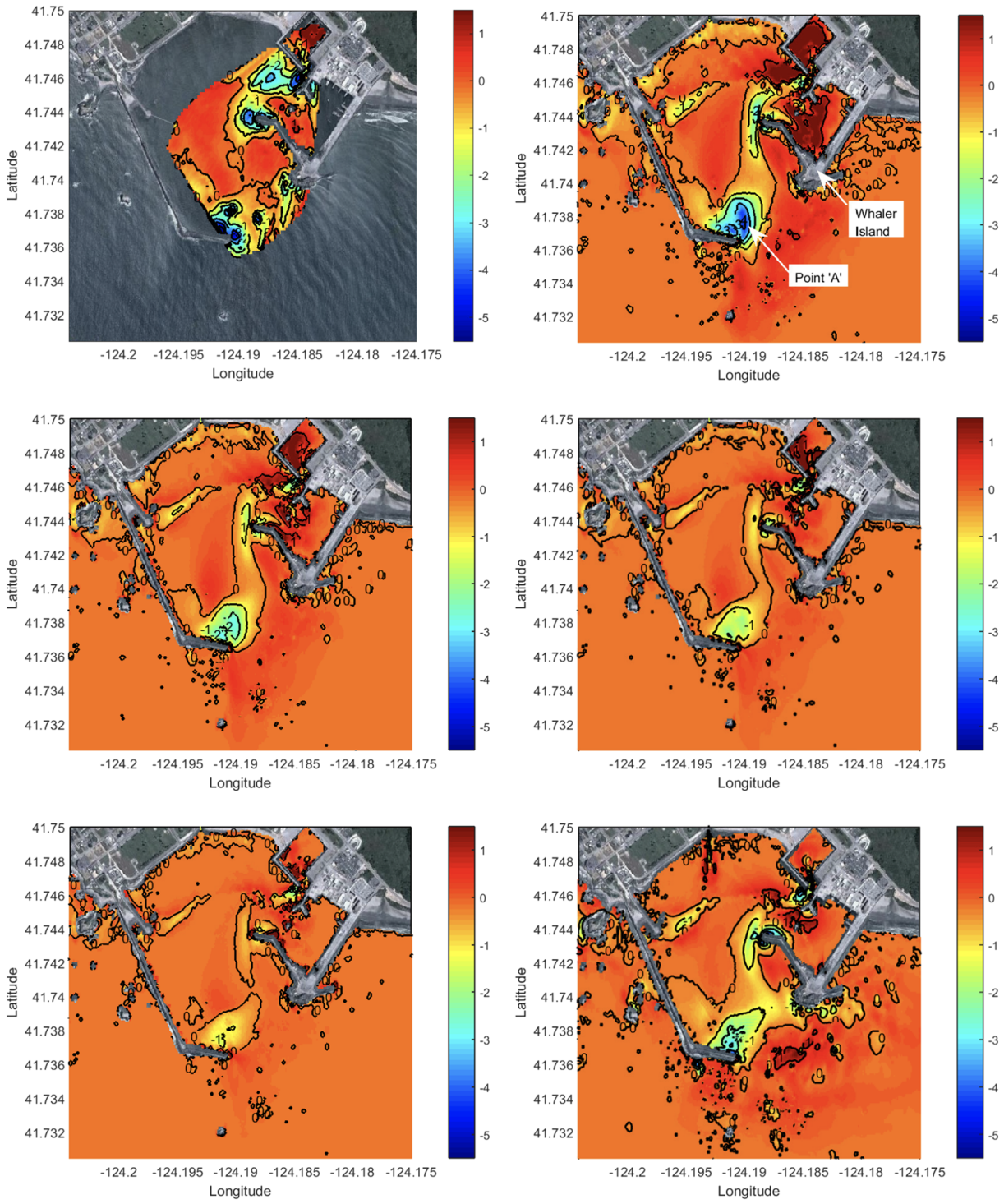

Figure 15. Observed (upper left; data from Wilson *et al.*, 2012) and computed (upper right for D_{50} = 0.15 mm; middle left for D_{50} = 0.25 mm; middle right for D_{50} = 0.35 mm; lower left for D_{50} = 0.50 mm; lower right for D_{50} = 0.25 mm using SWE model) bathymetric changes at Crescent City Harbor (numbers in metric units; background image is from Google Earth; point A in upper right plot is specified for Figure 19). [Colour figure can be viewed at wileyonlinelibrary.com]

to the strong current field formed by geometric contraction. Specifically, near the edge of the jetty in the outer harbour entrance and Whaler Island, very energetic flows induce sediment movement. In those areas, the erosion flux is larger than the deposition flux at the studied time, which will eventually cause scouring around the structures. Moving sediment particles settle down in the centre of the harbour basin, where the flow slows due to the sudden expansion of the waterway and increasing water depth. A similar process is repeated during tsunami wave retraction out of the harbour basin. These sedimentation characteristics are also addressed by Wilson *et al.* (2012), confirming the present simulation results. More details on tsunami-related sedimentation will be discussed in the following section.

Discussion of the Morphologic Changes Caused by Tsunamis

A widespread and profound effect of tsunamis on coastal morphology has been revealed through field observations (e.g. Nishimura and Miyaji, 1995; Moore *et al.*, 2006; Paris *et al.*, 2009; Goto *et al.*, 2011; Wilson *et al.*, 2012), as well as

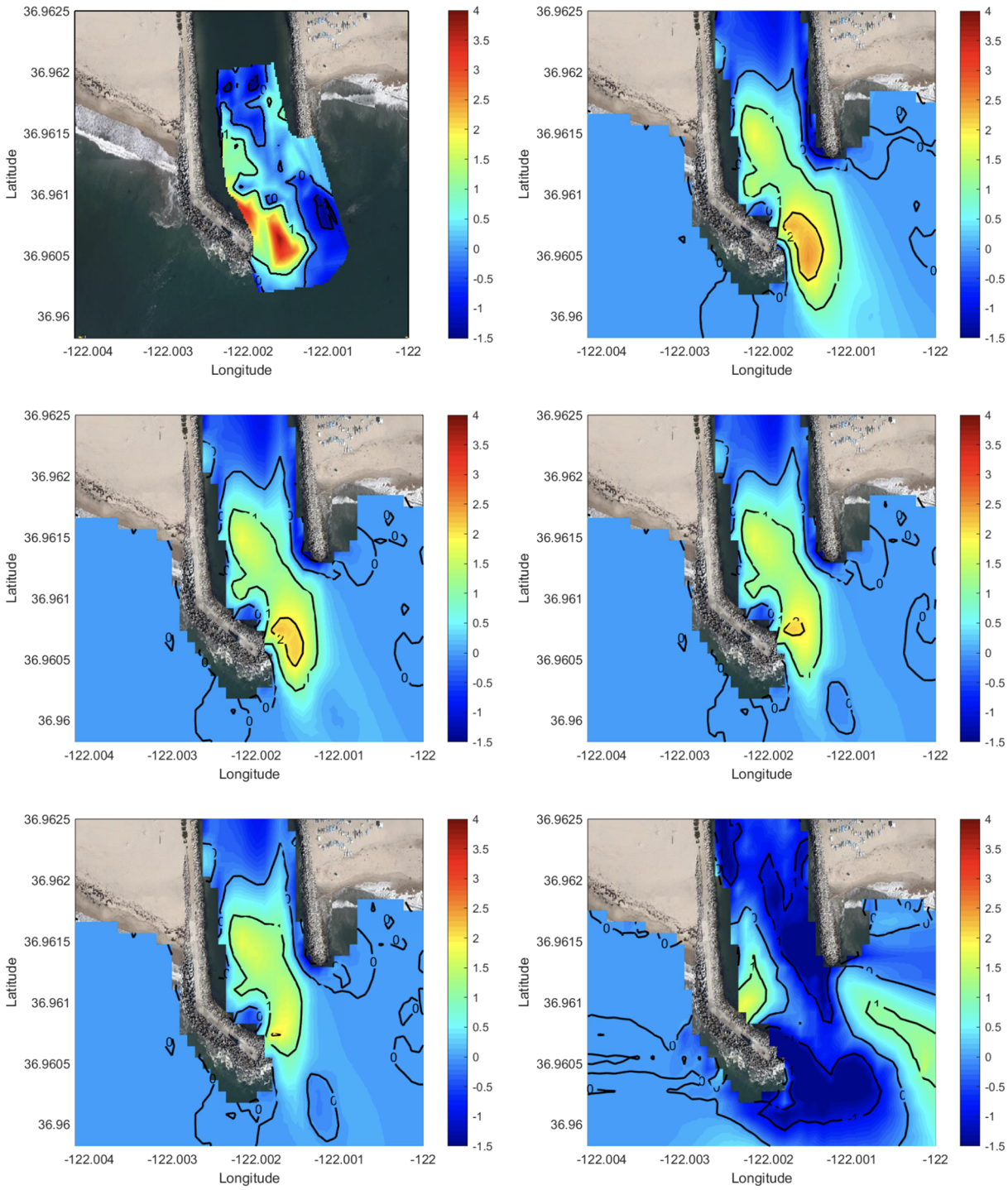

Figure 16. Observed (upper left; data from Wilson *et al.*, 2012) and computed (upper right for D_{50} = 0.15 mm; middle left for D_{50} = 0.25 mm; middle right for D_{50} = 0.35 mm; lower left for D_{50} = 0.50 mm; lower right for D_{50} = 0.15 mm using SWE model) bathymetric changes at Santa Cruz Harbor (numbers in metric units; background image is from Google Earth). [Colour figure can be viewed at wileyonlinelibrary.com]

Table II. Brier skill scores for different D_{50} values and hydrodynamic models.

	Crescent City Harbor		Santa Cruz Harbor	
D_{50} (mm).	Boussinesq	SWE	Boussinesq	SWE
0.15	0.30	−0.62	0.49	−1.05
0.25	0.43	0.41	0.60	−0.06
0.35	0.41	0.34	0.58	0.00
0.50	0.38	0.23	0.52	0.17

numerical tests (e.g. Apotsos *et al.*, 2011; Sugawara *et al.*, 2014). Generally, narrow or shallow coastal geometry amplifies the impacts of tsunamis on the bed materials. Tsunamis within a harbour create extremely strong currents (up to 7 m s^{-1} according to observations; Wilson *et al.*, 2012) and result in severe changes in bed morphology, which may take at least several months to recover. Such tsunami-related systematic processes on coastal morphology are reviewed in depth by Shiki *et al.* (2008).

In order to draw out the detailed processes of sedimentation caused by tsunami-induced currents, the time histories of

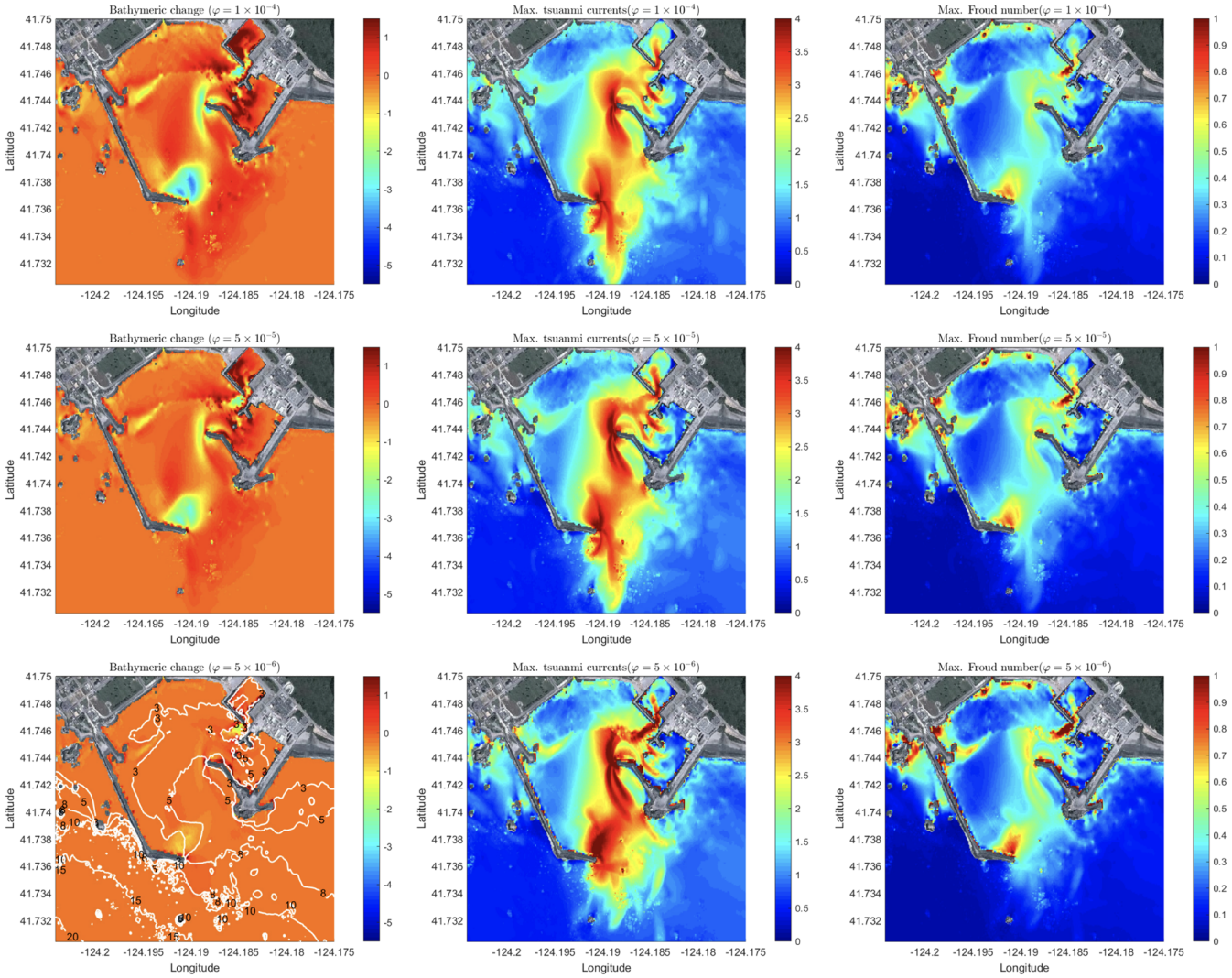

Figure 17. Maps for depth changes (left column), maximum tsunami currents (middle column), and maximum Froude numbers (right column) for different φ at Crescent City Harbor ($D_{50} = 0.25$ mm). Top panels for $\varphi = 1 \times 10^{-4}$, middle panels for $\varphi = 5 \times 10^{-5}$, bottom panels for $\varphi = 5 \times 10^{-6}$. White contour lines in the lower left panel represent bottom bathymetry. [Colour figure can be viewed at wileyonlinelibrary.com]

velocities, bathymetric changes, depth-averaged sediment concentrations, and net erosion fluxes ($=e-d$) at a particular point A (see Figure 15 for location) are extracted and compared, as shown in Figure 19. Coastal morphologic evolution mostly occurs during the initial 3–4 h of tsunami waves, without significant changes after. This tendency is also confirmed through an example shown in Sugawara *et al.* (2014). Thus, it can be inferred here that the physics of tsunami-induced sedimentation is confined to a time scale of *O*(hours). In general, such a time span of active sedimentation relies greatly on tsunami-induced currents, thus on tsunami sources. This source dependence has been pointed out by Lynett *et al.* (2014). They provided time-threshold maps of current speeds based on simulation results for different 60-h tsunami scenarios, implying that most of the maps are of *O*(hours). Therefore, considering that the initiation of sedimentation is critically related to the Shields parameter, and that the rapid currents are present only during the early stages of a tsunami, a time-based current map may be very useful for hazard mitigation planning, especially in scouring problems.

The dotted lines crossing plots in Figure 19 indicate different time spots of peak net erosion fluxes, leading to drastic depth changes. They reveal that energetic and erosive currents were introduced during both up- and down-rushing time (i.e. *v* in Figure 19a is either north- or southward, respectively). Consequently, strong currents generated substantial sediment concentrations, which quickly diminished in the subsequent wave phase as entrained sediments were transported out to a nearby deeper and wider zone.

A similar tentative idea of how tsunami deposition is created can be found in Shiki *et al.* (2008), who analysed tsunami hydrodynamics in four distinct stages: generation, propagation, inundation, and traction. In that context, it is emphasized that traction is the most important phase for the erosion process, since current with high sediment concentration occurs during this phase and thus sediment gravity-flow 'cocktails' (Bralower *et al.*, 1998) are produced. From a sedimentological perspective, the traction phase involving a tsunami-generated backwash current from shoreline to deep water can be seen as analogous to a process of wave undertow, in that both play a major role in offshore-directed transportation of sediments (see figure 10.1 in Dawson and Stewart, 2008). Finally, tsunami-induced currents with high sediment concentration transport sediment particles into a deeper zone before settling down, which offers a reasonable explanation for the tsunami depositions seen in the near vicinity of point A.

Other notable signatures found in tsunami-related sedimentation exist, such as basal unconformity, landward fining sequence, fining upward sequence, distinctive layering, and so on (Mamo *et al.*, 2009). Therefore, these tsunami signatures may be significant in assisting an understanding of tsunami-related sedimentation; however, they are best elucidated in

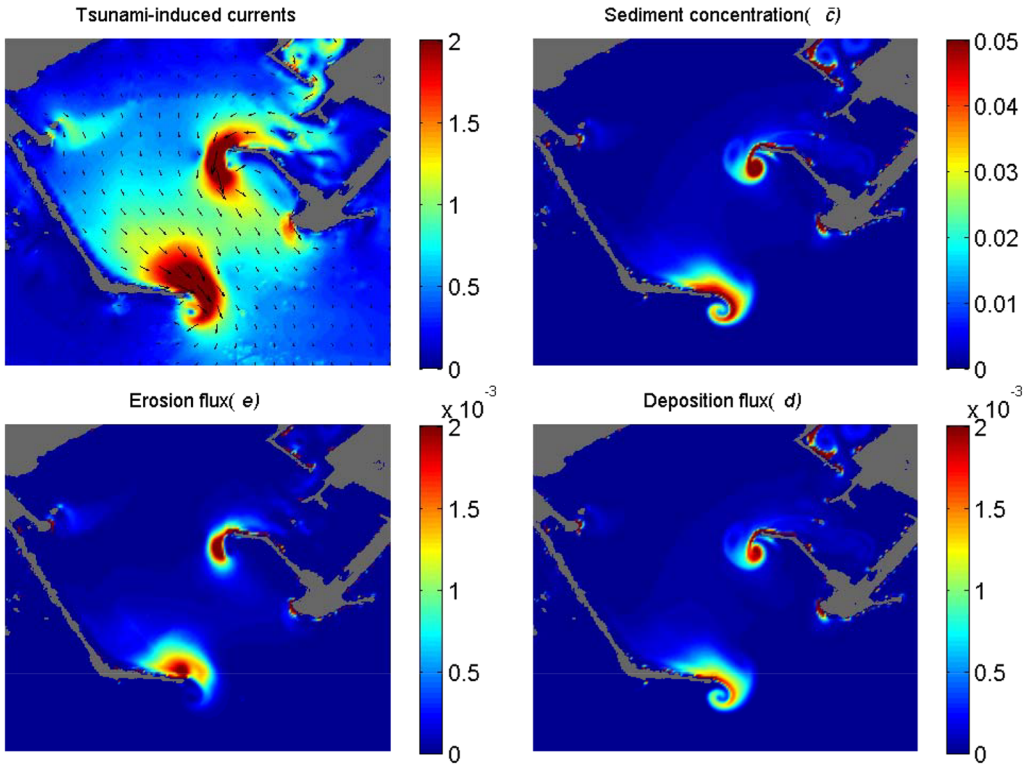

Figure 18. Numerical results of bathymetric changes in Crescent City Harbor at time $t = 637$ min since EQ; flow speed with velocity vectors (m s^{-1}) (upper left), depth-averaged sediment concentration (–) (upper right), erosion flux (m s^{-1}) (lower left), and deposition flux (m s^{-1}) (lower right). [Colour figure can be viewed at wileyonlinelibrary.com]

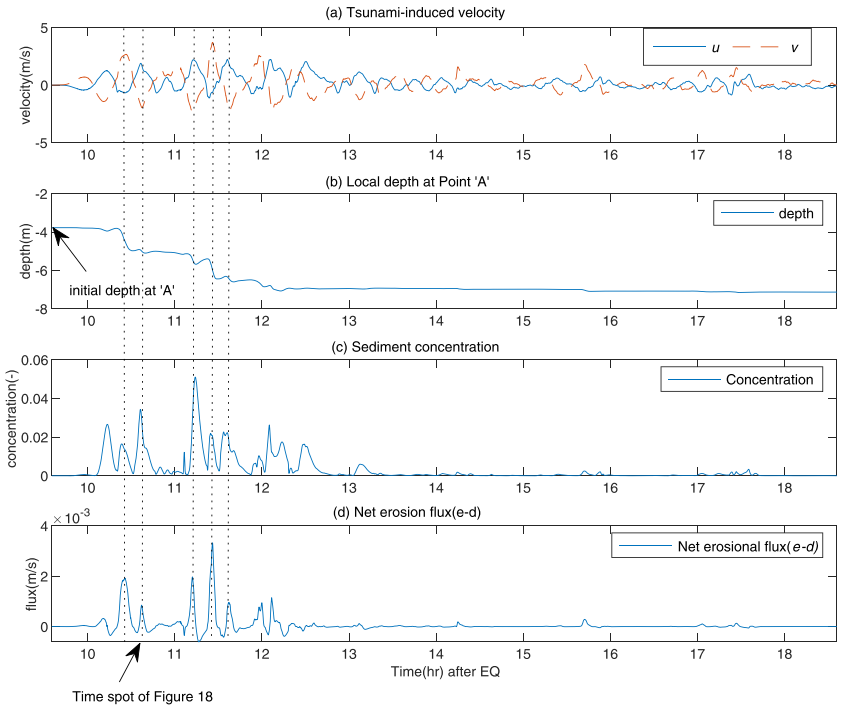

Figure 19. Calculated time history of (a) velocity, (b) local depth, (c) sediment concentration, and (d) net erosion flux at local point A (see Figure 15 for location) during tsunami events: u and v in (a) represent longitudinal and latitudinal velocity, respectively. [Colour figure can be viewed at wileyonlinelibrary.com]

detail through depth-resolving (3D) analysis with multi-class sediment transport, which is beyond the scope of this study.

Nevertheless, the sediment processes that are not fully accounted for by closures involved in the present model can be accommodated extensively by the empirical parameter φ. Based on the applied values and sensitivity tests, φ is found to have a large influence on the results, suggesting that it is dependent on the nature of the bed materials; the use of high φ [i.e. $O(10^{-3})$] holds for morphodynamic changes of relatively light bed materials (i.e. specific gravity of 1.5 in case 1), while a relatively smaller value of φ [i.e. $O(10^{-6} \sim 10^{-5})$] is recommended for particles having specific gravity similar to that of

natural sand. Meanwhile, the application of different φ values produced equally different effects on surface wave motions, and thus different interactions between hydrodynamics and morphodynamics. Thereby, it is also important to note that an appropriate value for φ needs to be determined considering not only morphodynamic condition, but also hydrodynamic condition.

Another important process to take into account through φ is the high sediment concentration and resulting density stratification, since this may affect both hydrodynamic and morphodynamic processes (e.g. Richardson and Zaki, 1954; Winterwerp, 2001). In order to figure out if the empirical parameter φ can possibly be utilized to account for the additional process by high sediment concentration such as hindered settling – and thus we may be able to detail it in our model – we looked at the sediment evolutions in case 1 and the Tohoku-oki tsunami case. From Figure 3, where different φ values were set, we can first see that the concentration is generated differently by different φ. For large φ, high sediment concentration is generated while the flow velocity decreases in comparison with those for small φ. Similarly, maximum sediment concentrations for different φ in the Tohoku-oki tsunami simulation are shown in Figure S2, revealing that while in most of the area (except very near the shoreline) sediment concentration is below 0.2, the degree of maximum concentration is determined by φ. Thus, density stratification formed by high sediment concentration is likely to be controlled by a large φ during the simulation. Finally, these results imply that the φ value itself can be utilized for controlling the sediment concentration, and thus the hindered settling process due to high sediment concentration is capable of being modelled in terms of a reduced φ. In such a case, however, the otherwise provided settling velocity calculated from Equation (17) is expected to be adaptively determined for consideration of the hindered settling process.

Conclusions

This study describes a numerical model for predicting morphodynamic changes caused by complex tsunami-induced currents of shallow, dispersive, and turbulent nature in the nearshore area. Through a two-way coupling technique, three sub-models, including a hydrodynamic model, a sediment transport model, and a morphodynamic model, are integrated to create a model framework for tsunami-caused sediment calculation. Since they are two-way coupled, bathymetric changes due to flow are able to affect fluid flow dynamics.

The Boussinesq model with bottom shear-induced rotational terms was selected as the hydrodynamic model because it provides highly accurate tsunami hydrodynamics in the nearshore (Son *et al.*, 2011; Lynett *et al.*, 2012; Borrero *et al.*, 2015). The primary advantage of the Boussinesq model is that it accurately describes complex nearshore hydrodynamics such as inundation, nonlinear wave interactions, and other turbulence-related activity. This results in more physically correct input to the sediment model.

The numerical discretization of the developed model is based on a finite-volume method, which is stable and suitable for long-term simulations. For the leading-order terms, both in the Boussinesq and sediment transport models, the MUSCL-TVD scheme coupled with the HLL Riemann solver was used. The model has been validated using typical sediment problems. One-dimensional or 2D test cases, containing dam-break flow or solitary wave propagations, were simulated and compared with laboratory data sets. Calculated results revealed good agreement with the experimental records when reasonable parameters were chosen. Even though the selection of parameters – such as the Manning coefficient and empirical parameter in each case – was calibrated based on previous studies and laboratory data when available, it should be noted that more physically reasonable values can be chosen without considering the best fit to the measurement.

Finally, the 2011 Tohoku-oki tsunami event, one of the most destructive tsunamis in history, was simulated with a focus on the localized effects of tsunami waves on sedimentation at the Crescent City Harbor and the Santa Cruz Harbor (USA). In these simulations, the multi-grid and multi-physics model developed by Son *et al.* (2011) was utilized to accurately reproduce the hydrodynamic environments during a tsunami event. The strong current fields in the harbour areas, including narrow waterways, were successfully generated. In conclusion, the simulated results of bathymetric changes during a tsunami event provide good approximations to the observed records (Wilson *et al.*, 2012). Detailed information about the sediment process is also revealed from the simulation results, which is consistent with the data from observations. Nevertheless, due to its heavy computational load in the field, application of state-of-the-art techniques such as GPU-accelerated modelling is expected to expedite the model implementation (e.g. Tavakkol and Lynett, 2017).

Additional simulations on sensitivity are performed in some cases and it is revealed that the effect with each higher-order or closure term may have a different impact on the sediment transport. For example, Figure 7 shows that the wave-breaking model's effects on sedimentation are quite limited, while the turbulence closure effects are more significant, as shown in Figure 9. Throughout Figures 3, 10, 17, and S2, the effect of the empirical parameter φ on the result is also described. Through the different types of sensitivity tests carried out so far, it can be concluded that φ may outweigh the effects of other higher-order or closure terms and thus it is regarded as a key controller in sediment modelling, which can primarily be determined around $O(10^{-6} \sim 10^{-5})$ for natural sand.

Acknowledgements—This research was supported by the SeeAt Programme funded by the Korea Meteorological Administration (KMI2018-09510) and by the Basic Science Research Programme through the National Research Foundation of Korea (NRF) funded by the Ministry of Education (2017R1D1A1B03031262).

Conflict of interest

The authors declare no conflict of interest.

References

Abderrezzak KEK, Paquier A. 2011. Applicability of sediment transport capacity formulas to dam-break flows over movable beds. *Journal of Hydraulic Engineering* **137**: 209–221.

Admire AR, Dengler LA, Crawford GB, Uslu BU, Borrero JC, Greer SD, Wilson RI. 2014. Observed and modeled currents from the Tohoku-oki, Japan and other recent tsunamis in northern California. *Pure and Applied Geophysics* **171**(12): 3385–3403.

Alsina J, Falchetti S, Baldock T. 2009. Measurements and modelling of the advection of suspended sediment in the swash zone by solitary waves. *Coastal Engineering* **56**: 621–631.

Apotsos A, Gelfenbaum G, Jaffe B. 2011. Process-based modeling of tsunami inundation and sediment transport. *Journal of Geophysical Research* **116**: F01006.

Bakhtyar B, Barry D, Li L, Jeng D, Yeganeh-Bakhtiary A. 2009. Modeling sediment transport in the swash zone: a review. *Ocean Engineering* **36**: 767–783.

Bjørkavåg M, Kalisch H. 2011. Wave breaking in Boussinesq models for undular bores. *Physics Letters A* **375**(14): 1570–1578.

Borrero JC, Lynett PJ, Kalligeris N. 2015. Tsunami currents in ports. *Philosophical Transactions of the Royal Society of London, Series A* **373**(2053): 20140372.

Bralower TJ, Paull CK, Leckie RM. 1998. The Cretaceous–Tertiary boundary cocktail: Chicxulub impact triggers margin collapse and extensive sediment gravity flows. *Geology* **26**: 331–334.

Cao Z, Pender G, Wallis S, Carling P. 2004. Computational dam-break hydraulics over erodible sediment bed. *Journal of Hydraulic Engineering* **130**: 689–703.

Capart H, Young DL. 1998. Formation of a jump by the dambreak wave over a granular bed. *Journal of Fluid Mechanics* **372**: 165–187.

Castro Díaz M, Fernández-Nieto E, Ferreiro A. 2008. Sediment transport models in shallow water equations and numerical approach by high order finite volume methods. *Computers & Fluids* **37**: 299–316.

Chen Q, Dalrymple RA, Kirby JT, Kennedy AB, Haller MC. 1999. Boussinesq modeling of a rip current system. *Journal of Geophysical Research: Oceans* **104**(C9): 20617–20637.

Cheng W, Weiss R. 2013. On sediment extent and runup of tsunami waves. *Earth and Planetary Science Letters* **362**: 305–309.

Dawson A, Shi S. 2000. Tsunami deposits. *Pure and Applied Geophysics* **157**: 875–897.

Dawson AG, Stewart I. 2008. Offshore tractive current deposition: the forgotten tsunami sedimentation process. In *Tsunamiites: features and implications*, Shiki T, Tsuji Y, Minoura K, Yamazaki T (eds). Elsevier: Amsterdam; 153–161.

Elder JW. 1959. The dispersion of marked fluid in turbulent shear flow. *Journal of Fluid Mechanics* **5**: 544–560.

Elfrink B, Baldock T. 2002. Hydrodynamics and sediment transport in the swash zone: a review and perspectives. *Coastal Engineering* **45**: 149–167.

Engel M, Oetjen J, May SM, Bruckner H. 2016. Tsunami deposits of the Caribbean: towards an improved coastal hazard assessment. *Earth-Science Reviews* **163**: 260–296.

Fraccarollo L, Capart H. 2002. Riemann wave description of erosional dam-break flows. *Journal of Fluid Mechanics* **461**: 183–228.

Fuhrman DR, Madsen PA. 2009. Tsunami generation, propagation, and run-up with a high-order Boussinesq model. *Coastal Engineering* **56** (7): 747–758.

Geist E, Lynett P, Chaytor J. 2009. Hydrodynamic modeling of tsunamis from the Currituck landslide. *Marine Geology* **264**(1–2): 41–52.

Goto K, Takahashi J, Oie T, Imamura F. 2011. Remarkable bathymetric change in the nearshore zone by the 2004 Indian Ocean tsunami: Kirinda Harbor, Sri Lanka. *Geomorphology* **127**: 107–116.

Goutiere L, Soares-Frazão S, Zech Y. 2012. Dam-break flow on mobile bed in abruptly widening channel: experimental data. *Journal of Hydraulic Research* **49**: 367–371.

Grilli ST, Ioualalen M, Asavanant J, Shi F, Kirby JT, Watts P. 2007. Source constraints and model simulation of the December 26, 2004, Indian Ocean Tsunami. *Journal of Waterway, Port, Coastal, and Ocean Engineering* **133**(6): 414–428.

Hinterberger C, Frohlich J, Rodi W. 2007. Three-dimensional and depth-averaged large eddy simulations of some shallow water flows. *Journal of Hydraulic Engineering* **133**: 857–872.

Horikawa K. 1981. Coastal sediment process. *Annual Review of Fluid Mechanics* **13**: 9–32.

Jaffe B, Goto K, Sugawara D, Gelfenbaum G, La Selle S. 2016. Uncertainty in tsunami sediment transport modeling. *Journal of Disaster Research* **11**(4): 647–661.

Kalligeris N, Skanavis V, Tavakkol S, Ayca A, Safty HE, Lynett P, Synolakis C. 2016. Lagrangian flow measurements and observations of the 2015 Chilean tsunami in Ventura, CA. *Geophysical Research Letters* **43**(10): 5217–5224.

Karambas T. 2006. Prediction of sediment transport in the swash-zone by using a nonlinear model. *Continental Shelf Research* **26**: 599–609.

Karambas T, Koutitas C. 2002. Surf and swash zone morphology evolution induced by nonlinear waves. *Journal of Waterway, Port, Coastal and Ocean Engineering* **128**(3): 102–113.

Kennedy A, Chen Q, Kirby J, Darlymple R. 2000. Boussinesq modeling of wave transformation, breaking, and runup. I: 1D. Journal of Waterway, Port. *Coastal and Ocean Engineering* **126**: 39–47.

Kim DH. 2015. H2D morphodynamic model considering wave, current and sediment interaction. *Coastal Engineering* **95**: 20–34.

Kim D, Lee S. 2012. Stable numerical model for transcritical flow and sediment transport on uneven bathymetry. *Journal of Hydraulic Engineering* **138**: 46–56.

Kim D, Lynett P, Socolofsky S. 2009. A depth-integrated model for weakly dispersive, turbulent, and rotational fluid flows. *Ocean Modeling* **27**(3–4): 198–214.

Kobayashi N, Johnson BD. 2001. Sand suspension, storage, advection, and settling in surf and swash zones. *Journal of Geophysical Research* **106**(C5): 9363–9376.

Kobayashi N, Lawrence A. 2004. Cross-shore sediment transport under breaking solitary waves. *Journal of Geophysical Research* **109**: C03047.

Lacy J, Rubin D, Buscombe D. 2012. Currents, drag, and sediment transport induced by tsunami. *Journal of Geophysical Research* **117**: C09028.

Lawrence J, Chadwick A, Fleming C. 2000. A phase-resolving model of sediment transport on coarse grained beaches. In Proceedings of the 27th International Conference on Coastal Engineering, Sydney, Australia; 624–636.

Li J, Qi M, Fuhrman DR. 2019. Numerical modeling of flow and morphology induced by a solitary wave on a sloping beach. *Applied Ocean Research* **82**: 259–273.

Li L, Qiu Q, Huang Z. 2012. Numerical modeling of the morphological change in Lhok Nga, west Banda Aceh, during the 2004 Indian Ocean tsunami: understanding tsunami deposits using a forward modeling method. *Natural Hazards* **64**: 1549–1574.

Lynett P, Borrero J, Weiss R, Son S, Greer D, Renteria W. 2012. Observations and modeling of tsunami-induced currents in ports and harbors. *Earth and Planetary Science Letters* **327–328**: 68–74.

Lynett P, Borrero J, Son S, Wilson R, Miller K. 2014. Assessment of the tsunami-induced current hazard. *Geophysical Research Letters* **41**: 2048–2055.

Mamo B, Strotz L, Dominey-Howes D. 2009. Tsunami sediments and their foraminiferal assemblages. *Earth-Science Reviews* **96**: 263–278.

Marsooli R, Wu W. 2014. Three-dimensional numerical modeling of dam-break flows with sediment transport over movable beds. *Journal of Hydraulic Engineering* **141**(1): 04014066.

Moore A, Nishimura Y, Gelfenbaum G, Kamataki T, Triyono R. 2006. Sedimentary deposits of the 26 December 2004 tsunami on the northwest coast of Aceh, Indonesia. *Earth, Planets and Space* **58**(2): 253–258.

Nishimura Y, Miyaji N. 1995. Tsunami deposits from the 1993 southwest Hokkaido earthquake and the 1640 Hokkaido Komagatake eruption, northern Japan. *Pure and Applied Geophysics* **144**(3–4): 719–733.

Papanicolaou A, Elhakeem M, Krallis G, Prakash S, Edinger J. 2008. Sediment transport modeling review – current and future developments. *Journal of Hydraulic Engineering* **134**(1): 1–14. https://doi.org/10.1061/(ASCE)0733-9429(2008)134:1(1).

Paris R, Wassmer P, Sartohadi J, Lavigne F, Barthomeuf B, Desgages E, Grancher D, Baumert P, Vautier F, Brunstein D, Gomez C. 2009. Tsunamis as geomorphic crises: lessons from the December 26, 2004 tsunami in Lhok Nga, west Banda Aceh (Sumatra, Indonesia). *Geomorphology* **104**(1): 59–72.

Ponce VM. 1989. *Engineering Hydrology, Principles and Practices*. Englewood Cliffs, NJ: Prentice Hall.

Postacchini M, Brocchini M, Mancinelli A, Landon M. 2012. A multipurpose, intra-wave, shallow water hydro-morphodynamic solver. *Advances in Water Resources* **38**: 13–26.

Rakha K, Deigaard R, Broker I. 1997. A phase-resolving cross shore sediment transport model for beach profile evolution. *Coastal Engineering* **31**: 231–261.

Raubenheimer B. 2002. Observations and predictions of fluid velocities in the surf and swash zones. *Journal of Geophysical Research* **107** (C11): 11-1–11-7.

Richardson JF, Zaki WN. 1954. The sedimentation of a suspension of uniform spheres under conditions of viscous flow. *Chemical Engineering Science* **3**(2): 65–73.

Roelvink JA. 2006. Coastal morphodynamic evolution techniques. *Coastal Engineering* **53**: 277–287.

Saengsupavanich C, Chonwattana S, Naimsampao T. 2009. Coastal erosion through integrated management: a case of Southern Thailand. *Ocean & Coastal Management* **52**(6): 307–316.

Scheffers A, Kelletat D. 2003. Sedimentologic and geomorphologic tsunami imprints worldwide – a review. *Earth-Science Reviews* **63**: 83–92.

Shi F, Vittori G, Kirby JT. 2015. Concurrent correction method for modeling morphological response to dredging an offshore sandpit. *Coastal Engineering* **97**: 1–10.

Shiki T, Tsuji Y, Yamazaki T, Minoura K. 2008. *Tsunamiites: Features and Implications*. Elsevier: Amsterdam.

Shimozono T, Sato S, Tajima Y. 2007. Numerical study of tsunami run-up over erodible sand dunes. In Proceedings of Coastal Sediments'07, New Orleans; 1089–1102.

Son S, Lynett P. 2014. Interaction of dispersive water waves with weakly sheared currents of arbitrary profile. *Coastal Engineering* **90**: 64–84.

Son S, Lynett P, Kim D. 2011. Nested and multi-physics modeling of tsunami evolution from generation to inundation. *Ocean Modelling* **38** (1–2): 96–113.

Sugawara D, Goto K, Jaffe E. 2014. Numerical models of tsunami sediment transport – current understanding and future directions. *Marine Geology* **352**: 295–320.

Sukhodolov AN, Rhoads BL. 2001. Field investigation of three-dimensional flow structure at stream confluences: 2. *Turbulence. Water Resources Research* **37**(9): 2411–2424.

Sutherland J, Peet AH, Soulsby R. 2004. Evaluating the performance of morphological models. *Coastal Engineering* **51**(8–9): 917–939.

Tavakkol S, Lynett P. 2017. Celeris: a GPU-accelerated open source software with a Boussinesq-type wave solver for real-time interactive simulation and visualization. *Computer Physics Communications* **217**: 117–127.

Tomita T, Imamura F, Arikawa T, Yasuda T, Kawata Y. 2006. Damage caused by the 2004 Indian Ocean tsunami on the southeasten coast of Sri Lanka. *Coastal Engineering Journal* **48**(2): 99–116.

Tyldesley JR. 1973. *An Introduction to Tensor Analysis: For Engineers and Applied Scientists*. Longman: Harlow.

van Dongeren A, van Ormondt M, Sembiring L, Sasso R, Austin M, Briere C, Swinkels C, Roelvink JA, van Thiel de Vries JSM. 2013. Rip current predictions through model-data assimilation on two distinct beaches. In Coastal Dynamics 2013: 7th International Conference on Coastal Dynamics, Arcachon, France; 1775–1786.

van Rijn LC, Walstra DJR, Grasmeijer B, Sutherland J, Pan S, Sierra JP. 2003. The predictability of cross-shore bed evolution of sandy beaches at the time scale of storms and seasons using process-based profile models. *Coastal Engineering* **47**: 295–327.

Wei G, Kirby JT, Grilli ST, Subramanya R. 1995. A fully nonlinear Boussinesq model for surface waves. Part 1. Highly nonlinear unsteady waves. *Journal of Fluid Mechanics* **294**: 71–92.

Weiss R, Bourgeois J. 2012. Understanding sediments – reducing tsunami risk. *Science* **336**(6085): 1117–1118.

Wilson R, Davenport C, Jaffe B. 2012. Sediment scour and deposition within harbors in California (USA), caused by the March 11, 2011 Tohoku-oki tsunami. *Sedimentary Geology* **282**: 228–240.

Winterwerp JC. 2001. Stratification effects by cohesive and noncohesive sediment. *Journal of Geophysical Research: Oceans* **106**(C10): 22559–22574.

Wu W, Wang S. 2007. One-dimensional modeling of dam-break flow over movable beds. *Journal of Hydraulic Engineering* **133**: 48–58.

Wu W, Wang S. 2008. One-dimensional explicit finite-volume model for sediment transport with transient flows over movable beds. *Journal of Hydraulic Research* **46**(1): 87–98.

Wu W, Marsooli R, He Z. 2012. Depth-averaged two-dimensional model of unsteady flow and sediment transport due to noncohesive embankment break/breaching. *Journal of Hydraulic Engineering* **138**(6): 503–516.

Xiao J, Lin B, Falconer R, Wang G. 2010. Modelling dam-break flows over mobile beds using a 2D coupled approach. *Advances in Water Resources* **33**: 171–183.

Yamashita K, Sugawara D, Takahashi T, Imamura F, Saito Y, Imato Y, Kai T, Uehara H, Kato T, Nakata K, Saka R. 2016. Numerical simulations of large-scale sediment transport caused by the 2011 Tohoku earthquake tsunami in Hirota Bay, southern Sanriku Coast. *Coastal Engineering Journal* **58**(04) 1640015.

Yoon H-D, Cox D. 2010. Large-scale laboratory observations of wave breaking turbulence over an evolving beach. *Journal of Geophysical Research* **115**: C10007.

Yoshii T, Tanaka S, Matsuyama M. 2017. Tsunami deposits in a super-large wave flume. *Marine Geology* **391**: 98–107.

Zhang Y, Kennedy A, Panda N, Dawson C, Westerlink J. 2013. Boussinesq–Green–Naghdi rotational water wave theory. *Coastal Engineering* **73**: 13–27.

Zhou JG, Causon DM, Mingham CG, Ingram DM. 2001. The surface gradient method for thetreatment of source terms in the shallow-water equations. *Journal of Computational Physics* **168**(1): 1–25.

Supporting Information

Additional supporting information may be found online in the Supporting Information section at the end of the article.

Data S1 Supporting Information